



**Fermi National Accelerator Laboratory**

**FERMILAB-Pub-95/298-E**

**E672 and E706**

**Production of  $J/\psi$  and  $\psi$  (2S) Mesons in  
 $\pi^-$  Be Collisions at 515 GeV/c**

A. Gribushin et al.

The E672 and E706 Collaborations

*Fermi National Accelerator Laboratory  
P.O. Box 500, Batavia, Illinois 60510*

September 1995

Submitted to *Physical Review D*

## Disclaimer

*This report was prepared as an account of work sponsored by an agency of the United States Government. Neither the United States Government nor any agency thereof, nor any of their employees, makes any warranty, expressed or implied, or assumes any legal liability or responsibility for the accuracy, completeness, or usefulness of any information, apparatus, product, or process disclosed, or represents that its use would not infringe privately owned rights. Reference herein to any specific commercial product, process, or service by trade name, trademark, manufacturer, or otherwise, does not necessarily constitute or imply its endorsement, recommendation, or favoring by the United States Government or any agency thereof. The views and opinions of authors expressed herein do not necessarily state or reflect those of the United States Government or any agency thereof.*

# PRODUCTION OF $J/\psi$ AND $\psi(2S)$ MESONS IN $\pi^-$ Be COLLISIONS AT 515 GeV/c

A. Gribushin,<sup>4</sup> V. Abramov,<sup>2</sup> Yu. Antipov,<sup>2</sup> B. Baldin,<sup>2</sup> R. Crittenden,<sup>4</sup> C. Davis,<sup>5</sup>  
L. Dauwe,<sup>6</sup> S. Denisov,<sup>2</sup> A. Dyshkant,<sup>2</sup> A. Dzierba,<sup>4</sup> V. Glebov,<sup>2</sup> H. Goldberg,<sup>3</sup> R. Jesik,<sup>3</sup>  
V. Koreshev,<sup>2</sup> J. Krider,<sup>1</sup> A. Krinitsyn,<sup>2</sup> R. Li,<sup>4</sup> S. Margulies,<sup>3,†</sup> T. Marshall,<sup>4</sup> J. Martin,<sup>4</sup>  
H. Mendez,<sup>3</sup> A. Petrukhin,<sup>2</sup> J. Solomon,<sup>3</sup> V. Sirotenko,<sup>2</sup> P. Smith,<sup>4</sup> T. Sulanke,<sup>4</sup>  
R. Sulyaev,<sup>2,†</sup> F. Vaca,<sup>3</sup> A. Ziemiński<sup>4</sup>

(E672 Collaboration)

S. Blusk,<sup>12</sup> C. Bromberg,<sup>9</sup> P. Chang,<sup>10</sup> B. Choudhary,<sup>8</sup> W.H. Chung,<sup>12</sup> L. de Barbaro,<sup>13</sup>  
W. Długosz,<sup>10</sup> J. Dunlea,<sup>13</sup> E. Engels, Jr.,<sup>12</sup> G. Fanourakis,<sup>13</sup> G. Ginther,<sup>13</sup> K. Hartman,<sup>11</sup>  
J. Huston,<sup>9</sup> V. Kapoor,<sup>8</sup> C. Lirakis,<sup>10</sup> S. Mani,<sup>7</sup> J. Mansour,<sup>13</sup> A. Maul,<sup>9</sup> R. Miller,<sup>9</sup>  
B.Y. Oh,<sup>11</sup> E. Pothier,<sup>10</sup> R. Roser,<sup>13</sup> P. Shepard,<sup>12</sup> D. Skow,<sup>1</sup> P. Slattey,<sup>13</sup> L. Sorrell,<sup>9</sup>  
W. Toothacker,<sup>11</sup> N. Varelas,<sup>13</sup> D. Weerasundara,<sup>12</sup> J. Whitmore<sup>11</sup> C. Yosef,<sup>9</sup> M. Zieliński<sup>13</sup>

(E706 Collaboration)

<sup>1</sup>*Fermi National Accelerator Laboratory, Batavia, Illinois 60510*

<sup>2</sup>*Institute for High Energy Physics, Serpukhov, Russia*

<sup>3</sup>*University of Illinois at Chicago, Chicago, Illinois 60607*

<sup>4</sup>*Indiana University, Bloomington, Indiana 47405*

<sup>5</sup>*University of Louisville, Louisville, Kentucky 40292*

<sup>6</sup>*University of Michigan at Flint, Flint, Michigan 48502*

<sup>7</sup>*University of California-Davis, Davis, California 95616*

<sup>8</sup>*University of Delhi, Delhi, India 110007*

<sup>9</sup>*Michigan State University, East Lansing, Michigan 48824*

<sup>10</sup>*Northeastern University, Boston, Massachusetts 02115*

<sup>11</sup>*Pennsylvania State University, University Park, Pennsylvania 16802*

<sup>12</sup>*University of Pittsburgh, Pittsburgh, Pennsylvania 15260*

<sup>13</sup>*University of Rochester, Rochester, New York 14627*

<sup>‡</sup>*Deceased*

## Abstract

We have studied the production of  $J/\psi$  and  $\psi(2S)$  charmonium mesons in 515 GeV/c  $\pi^-$  Be collisions in the Feynman- $x$  range  $0.1 < x_F < 0.8$ .  $J/\psi$  mesons were detected via their decay into  $\mu^+\mu^-$ , and  $\psi(2S)$  mesons were studied in both the  $\mu^+\mu^-$  and  $J/\psi\pi^+\pi^-$  decay modes.  $J/\psi$  differential cross sections have been measured as functions of  $x_F$ ,  $p_T^2$ , and the cosine of the Gottfried-Jackson decay angle. We measure an inclusive  $J/\psi$  cross section of  $Br(J/\psi \rightarrow \mu^+\mu^-) \cdot \sigma(\pi^-Be \rightarrow J/\psi + X)/A = (9.3 \pm 1.1(stat) \pm 1.1(sys))$  nb/nucleon for  $J/\psi$   $x_F > 0.1$ . Our results are compared with those from other experiments performed at lower beam energies. We also measure differential  $\psi(2S)$  cross sections as functions of  $x_F$  and  $p_T^2$ , and a cross section of  $Br(\psi(2S) \rightarrow J/\psi\pi^+\pi^-) \cdot \sigma(\pi^-Be \rightarrow \psi(2S) + X)/A = (7.4 \pm 1.5(stat) \pm 1.2(sys))$  nb/nucleon for  $\psi(2S)$   $x_F > 0.1$ . The fraction of the inclusive  $J/\psi$  yield due to  $\psi(2S)$  meson decays is  $0.083 \pm 0.017(stat) \pm 0.013(sys)$ , and the ratio of  $\psi(2S)$  decay rates is  $Br(\psi(2S) \rightarrow J/\psi\pi^+\pi^-)/Br(\psi(2S) \rightarrow \mu^+\mu^-) = 30.2 \pm 7.1(stat) \pm 6.8(sys)$ . We have searched for production of “hidden” charm resonances decaying into either  $J/\psi\pi^\pm$ ,  $\psi(2S)\pi^\pm$ , or  $J/\psi\pi^+\pi^-$  systems. We report an upper limit of 3.1 nb/nucleon for the product of branching ratio and cross section for the recently reported enhancement at a  $J/\psi\pi^+\pi^-$  mass of 3.836 GeV/c<sup>2</sup>.

PACS numbers 13.85.Ni, 25.40.Ve, 25.80.Ls

Typeset using REVTeX

## I. INTRODUCTION

The hadronic production of charmonium states, and  $J/\psi$  in particular, continues to play a role in the study of perturbative and non-perturbative Quantum Chromodynamics (QCD) [1,2]. A significant fraction of the  $J/\psi$ s produced in hadronic interactions comes from the decay of higher mass charmonium states. One of the goals of this experiment is the measurement of the cross section for several charmonium states,  $J/\psi$ ,  $\psi(2S)$ , and  $\chi_c$ , and a comparison between these values and theoretical predictions using various models of parton and final-state interactions.

In addition to QCD studies, charmonium hadroproduction provides spectroscopic information complementary to that obtained in  $e^+e^-$  interactions. The initial states produced in hadronic collisions are not restricted to those with the quantum numbers of the photon as in  $e^+e^-$  interactions.

In this paper we report  $J/\psi$  and  $\psi(2S)$  total and differential cross sections, measurements of the fraction of the inclusive  $J/\psi$  yield due to  $\psi(2S)$  decay, the ratio of the  $\psi(2S)$  decay rates into  $J/\psi\pi^+\pi^-$  and  $\mu^+\mu^-$ , and results of a search for “hidden” charm resonances decaying into either  $J/\psi\pi^\pm$ ,  $\psi(2S)\pi^\pm$ , or  $J/\psi\pi^+\pi^-$  systems. In a subsequent paper we will discuss the cross sections for  $\chi_c$  and direct  $J/\psi$  production, and compare current models of QCD interactions to our results [3].

## II. APPARATUS

The experiment was performed in the Fermilab Meson West beam line using a large-aperture, open-geometry spectrometer with the capability of studying high-mass muon pairs. The layout of the experiment is shown in Fig. 1. A brief description of the essential elements of the Meson West apparatus as implemented in the 1990 run follows.

The beam line included a 42-m-long differential Cerenkov counter capable of tagging incident beam particles. The unseparated negative secondary 515 GeV/ $c$  beam was composed

primarily of pions with a small fraction ( $<5\%$ ) of kaons. The Cerenkov was not explicitly used in the analysis of the dimuon data described in this paper. The beam intensity varied during the data run and at its maximum was  $2 \times 10^8$  pions per 23-second-long spill (at 57 second intervals).

A hadron shield consisting of 5 m of iron was located upstream of the target to reduce background from off-axis hadrons and soft muons. One scintillator veto wall was placed upstream of the hadron shield and two more were located downstream of the shield. These veto walls were used to identify high energy muons that penetrated the iron. An on-line veto for the dimuon trigger rejected events containing coincidences between a signal from the upstream wall and a signal from at least one of the downstream walls.

Incident beam hadrons were defined by three scintillation counters (BA, BB, and BH) located upstream of the target and a three plane (X, Y, U) beam hodoscope with mm scale resolution. A beam particle was defined by signals from the BA and BB counters plus at least a two-fold coincidence from the hodoscope, and no signal from the BH beam hole counter. Signals from the beam hodoscope were also employed to veto events containing more than one spatially isolated beam particle. The redundancy in the beam trigger elements was employed to simultaneously satisfy timing requirements between dimuon and high- $p_T$  triggers.

The target consisted of two copper pieces each 0.8 mm thick, followed by two pieces of beryllium 3.71 cm and 1.12 cm thick separated by 1 cm. The total thickness of the target material corresponded to a 9% interaction length for pions.

Upstream of the target were three X-Y modules of silicon-strip detectors (SSDs) [4] which measured the trajectories of incident beam particles. Five more X-Y SSD modules followed the target. These modules were used to determine the trajectories of charged particles produced in the target and to reconstruct primary and secondary vertices. The first downstream SSD module was a hybrid with a 25- $\mu\text{m}$ -pitch inner region and a 50- $\mu\text{m}$ -pitch outer region; the remaining four modules had 50  $\mu\text{m}$  pitch throughout.

A dipole magnet imparting a  $p_T$  impulse of 0.45 GeV/ $c$  was located downstream of the

SSD system. Four proportional wire chamber (PWC) modules were located downstream of the magnet. Each module contained four wire planes to provide X, Y, U, and V measurements. (The U and V coordinates are a pair of orthogonal coordinates rotated by  $37^\circ$  relative to the X and Y coordinates.) The wires in each plane had a 2.54 mm pitch. An area of from 6 to 26 cm<sup>2</sup> in the center of each plane had reduced sensitivity to provide protection against noninteracting beam particles. Two stations of straw tube drift chambers [5], each with four planes in the X and four planes in the Y directions were located next to the outside PWC stations. In this analysis, momentum measurements for charged non-muon tracks employed the SSD system, the dipole magnet, and the PWCs, yielding a momentum resolution of  $\Delta p/p = 0.06\% p$ .

Interactions were detected by a pair of scintillation counters located before the dipole magnet and another pair after the magnet. An interaction was defined as a signal from at least two of these counters in coincidence with a valid beam particle signal. The interaction rate was generally less than 0.8 MHz.

A liquid-argon calorimeter (LAC) [6] was located downstream of the magnetic spectrometer. The LAC contained both electromagnetic and hadronic sections. The outer radius of the electromagnetic section was 1.65 m; the inner radius was 0.20 m. A helium-gas-filled pipe was located along the axis of the LAC to reduce interactions of beam particles. The total LAC material corresponded to more than 10 interaction lengths. Approximately 70% of the muons recorded in the muon detector passed through the axial beam pipe.

Downstream of the LAC was an iron/scintillator forward calorimeter instrumenting the acceptance region corresponding to the axial beam pipe in the LAC. This calorimeter had a diameter of 1 m with a 3 cm diameter axial beam hole and was 10 absorption lengths deep.

The dimuon detector [7,8] was located 20 m downstream of the target and extended for 16 m. The detector contained, in sequence, two muon PWC stations ( $\mu A$ ,  $\mu B$ ) with four planes each (X, Y, U, V), a beam dump consisting of tungsten and steel imbedded in concrete, an iron toroid magnet producing an average  $p_T$  impulse of 1.3 GeV/ $c$ , and four more PWCs ( $\mu 1 - \mu 4$ ) each with three planes (X, U, V). In these PWCs, the U and V coordinates were at

angles of  $45^\circ$  above and below the horizontal, respectively. Iron, lead and concrete shielding was interspersed between the  $\mu 1 - \mu 4$  chambers. Two muon hodoscope planes, H1 and H2, (each with sixteen petal-shaped scintillation counters) were also located in this region. The outer radius of the muon chambers and hodoscopes was 135 cm. The acceptance of the muon spectrometer was limited by tapered axial holes, ranging from 13 cm to 20 cm in radius, in the toroid magnet, muon chambers, and scintillator hodoscopes. The hole in the toroid was filled with lead absorber.

The muon detector was shielded from hadrons by material in the LAC, forward calorimeter, beam dump, toroid, and concrete shielding. Muons produced at the target required approximately 15 GeV to penetrate this material, and all particles reaching the muon hodoscopes were assumed to be muons. Two or more hits in each of the muon hodoscopes were required as part of a pretrigger [9]; the average hit multiplicity was 2.3. In addition to the muon hodoscope requirement, the previously cited on-line veto from the veto walls completed the pretrigger requirement. The pretrigger rate was  $2 \times 10^{-4}$  per live interaction. The pretrigger efficiency for two muons penetrating the system was 0.76 and remained constant over the data taking period. No radial dependence of the pretrigger counter efficiency was observed.

The final dimuon trigger was formed by the dimuon trigger processor (DMTP) which reconstructed space points in PWCs  $\mu 1$  and  $\mu 4$ , formed muon tracks (requiring an additional hit in either  $\mu 2$  or  $\mu 3$  along the projected track trajectory), measured their momenta from the estimated bend in the toroid (assuming that the tracks originated in the target), and calculated the dimuon invariant mass. Trajectories of muon tracks reconstructed in the downstream muon PWCs were projected toward the center of the target. The processor accepted only muon tracks with at least three hits in each of the  $\mu A$  and  $\mu B$  chambers within assigned roads around the projected trajectory. A trigger resulted if any of the dimuon masses, calculated assuming massless muons, was above a preset threshold. A mass threshold of  $0.7 \text{ GeV}/c^2$  resulted in a trigger rate of  $2 \times 10^{-5}$  per live interaction. The average DMTP processing time was  $10 \mu\text{s}$  per pretrigger, which included  $5 \mu\text{s}$  to decode the



muon chamber data. The combined efficiency of the chambers and the DMTP algorithm was 0.77 for dimuon events. The DMTP mass resolution for the  $J/\psi$  was  $550 \text{ MeV}/c^2$ .

### III. DATA

Approximately  $5 \times 10^6$  dimuon triggers were recorded during the 1990 run (corresponding to a luminosity of  $7.5 \text{ pb}^{-1}$  per nucleon on Be), yielding  $3 \times 10^5$  events with reconstructed dimuon combinations originating from the target region. For each dimuon triggered event, a fit was performed to link muon tracks through the entire detector. This fit included multiple-scattering considerations and a consistency requirement for the track momentum as analyzed via the dipole magnet and by the toroid. Only events with at least two fully-linked muons were retained. The remaining segments in the SSDs and upstream PWCs were used to find other tracks and event vertices. The distribution of the reconstructed primary vertex along the incident beam (Z) direction for events containing reconstructed  $J/\psi$ s is shown in Fig. 2.

Dimuons contributing to this analysis come from events with primary vertices in the Be target, and have dimuon Feynman- $x$  ( $x_F = 2p_z/\sqrt{s}$ ) in the range  $0.1 < x_F < 0.8$ . Figures 3 and 4 show the reconstructed opposite-sign dimuon invariant mass distributions for the full mass range and in the  $J/\psi$  region, respectively. A fit to the high-mass sample yields  $9600 \pm 105(\text{stat}) \pm 200(\text{sys})$   $J/\psi$ s with a FWHM mass resolution of  $160 \text{ MeV}/c^2$ , and  $270 \pm 35(\text{stat}) \pm 50(\text{sys})$   $\psi(2\text{S})$ s. The fit used resolution functions determined by Monte Carlo simulations for the  $J/\psi$  and  $\psi(2\text{S})$  resonances plus the sum of two exponentials for the continuum background. The  $J/\psi$  mass obtained from the fit is  $(3.0975 \pm 0.0003) \text{ GeV}/c^2$ . The  $\psi(2\text{S})$  mass was fixed at the PDG value [10]. The systematic uncertainties in the number of  $J/\psi$  and  $\psi(2\text{S})$  events take into account variations in the assumed shapes for the signal and background distributions.

To determine overall reconstruction efficiencies and acceptance, we generated  $3 \times 10^5$  Monte Carlo  $J/\psi$  events. The  $x_F$  and  $p_T^2$  distributions for the Monte Carlo  $J/\psi$ s were taken from our previous measurement [8]. We assumed that  $J/\psi$ s decay isotropically (con-

sistent with observations described subsequently). The Monte Carlo events also contained underlying charged tracks with an average multiplicity matching the data. The dimuons and associated particles were propagated through a GEANT simulation of the Meson West spectrometer, which incorporated measured spectrometer chamber efficiencies and instrumental noise taken from real data. The dimuon events were then processed with the same tracking programs as used on the data. We have evaluated  $J/\psi$  reconstruction efficiency and geometrical acceptance as a function of three variables: (i)  $J/\psi$  Feynman- $x$ ,  $x_F$ , (ii)  $J/\psi$  transverse momentum squared,  $p_T^2$ , and (iii) the cosine of the Gottfried-Jackson decay angle between the  $\mu^+$  and the beam axis in the  $J/\psi$  rest frame,  $\cos \theta$ . The product of acceptance and reconstruction efficiency,  $a_{J/\psi \rightarrow \mu^+ \mu^-} \cdot \epsilon_{J/\psi \rightarrow \mu^+ \mu^-}$ , was calculated (a) as a two-dimensional surface over the  $x_F$  and  $p_T^2$  plane (see Fig. 5), and (b) by an iterative method with the Monte Carlo  $x_F$  and  $p_T^2$  distributions adjusted to match those determined from the data after each iteration (see Figs. 6a and 6b). The two methods gave consistent cross section results. The product of acceptance and efficiency as a function of  $\cos \theta$ , integrated over the  $x_F$  and  $p_T^2$  spectra, is shown in Fig. 6c.

#### IV. $J/\psi$ DIFFERENTIAL CROSS SECTIONS

In Fig. 7 we present  $J/\psi$  differential distributions with empirical fits. Data points were corrected for the geometrical acceptance and reconstruction efficiencies discussed above.  $J/\psi$ s were defined as opposite sign dimuons with invariant mass between 2.8 GeV/ $c^2$  and 3.4 GeV/ $c^2$ . With the constraint that the  $\mu^+ \mu^-$  invariant mass is 3.097 GeV/ $c^2$ , and that the two muons come from the same vertex, a two constraint kinematic fit was done for each dimuon to improve the muon momentum resolution. The  $x_F$  resolution for fitted  $J/\psi$ s varied from 0.005 at  $x_F = 0.2$  to 0.03 at  $x_F = 0.7$ . As a consequence of this constrained fit we have not performed background subtraction for the  $J/\psi$  differential distributions. The background accounts for 8% of the combinations in this mass range and this fraction does not change appreciably as a function of  $x_F$  and  $p_T^2$ .

The Feynman- $x$  acceptance of the apparatus does not allow for an independent determination of the differential cross section behavior for  $x_F < 0.1$ . We used the following parameterization to describe  $d\sigma/dx_F$  [11] (see Fig. 7a):

$$d\sigma/dx_F \propto x_1^a (1-x_1)^\kappa (1-x_2)^{\kappa+2} / (x_1+x_2), \quad (4.1)$$

where

$$x_{1,2} = 0.5[\sqrt{x_F^2 + 4\tau} \pm x_F], \quad (4.2)$$

and  $\tau = M_{J/\psi}^2/s$ . Here,  $x_1$  represents the beam parton relative momentum and  $x_2$  the target parton relative momentum. The values obtained from the fit are  $\kappa = 2.19 \pm 0.10$  and  $a = 0.33 \pm 0.06$ , with  $\chi^2/ndf = 30/32$ . The empirical factor  $x_1^a$  in Eq. 4.1, which was not used in ref. [11], was introduced to improve the fit in the low- $x_F$  region. A fit with  $a$  set to zero gives  $\kappa = 1.69 \pm 0.04$  with  $\chi^2/ndf = 50/33$ .

The  $p_T^2$  spectrum (Fig. 7b) is fitted to the empirical form [12]

$$d\sigma/dp_T^2 \propto (1 + p_T^2/\beta^2)^c \quad (4.3)$$

with parameters  $\beta = 2.3 \pm 0.2$  and  $c = -4.7 \pm 0.6$  resulting in  $\chi^2/ndf = 61/47$ . Fig. 8 shows that the measured average  $p_T$  of the  $J/\psi$ ,  $\langle p_T \rangle$ , is consistent with a slow decrease as a function of the  $J/\psi$   $x_F$ . The  $x_F$ -integrated value  $\langle p_T \rangle = 1.17 \pm 0.02$  GeV/ $c$  measured by this experiment is larger than the corresponding values reported at lower  $\sqrt{s}$ . As shown in Fig. 9, the value of  $\langle p_T \rangle$  grows linearly with the c.m. energy.

A fit to the  $\cos \theta$  distribution in the range  $|\cos \theta| < 0.8$  (Fig. 7c) with the function

$$d\sigma/d(\cos \theta) \propto (1 + \lambda \cos^2 \theta) \quad (4.4)$$

yields  $\lambda = -0.01 \pm 0.08$  and  $\chi^2/ndf = 33/34$ , which is consistent with unpolarized  $J/\psi$  production. Only 0.3% of the observed  $J/\psi$ s have  $|\cos \theta| > 0.8$ .

The  $J/\psi$  differential cross sections, shown in Figs. 7a-c, are tabulated in Table 1.

## V. $J/\psi$ INTEGRATED CROSS SECTION

The inclusive  $J/\psi$  cross section was determined as follows:

$$Br(J/\psi \rightarrow \mu^+\mu^-) \cdot \sigma(\pi^- Be \rightarrow J/\psi + X)/A = N_{J/\psi}^{(c)}/(L \cdot e_1 \cdot e_2). \quad (5.1)$$

Here,  $N_{J/\psi}^{(c)}$  is the measured number of  $J/\psi$ s coming from primary vertices corrected for geometrical acceptance and reconstruction efficiency on an event-by-event basis (see Fig. 5),  $L$  is the integrated luminosity,  $e_1$  is a luminosity correction factor, and  $e_2$  is an apparatus efficiency factor.

The integrated luminosity was calculated from the total number of beam particles incident on the 8.92 g/cm<sup>2</sup> Be target during the live time of the spectrometer. The luminosity correction factor,  $e_1$ , includes corrections for dimuon pretrigger and trigger processor dead time, losses due to timing requirements between the dimuon system and the rest of the spectrometer, and transverse target fiducial cuts. The apparatus efficiency factor,  $e_2$ , accounts for the pretrigger hodoscope and the dimuon trigger processor efficiencies mentioned in Section II.

The  $J/\psi$  cross section was evaluated for each of seven groups of data corresponding to different running conditions. The apparatus efficiency factor,  $e_2 = 0.59 \pm 0.05$ , remained constant during the data taking period. On the other hand, the luminosity correction factor,  $e_1$ , varied from 0.61 to 0.96, with a weighted average  $e_1 = 0.76$ . Nevertheless, the cross sections determined for individual groups agree with each other within uncertainties and the spread of the absolute values is less than 19%. A weighted average was used for the reported cross section.

For  $J/\psi$  with  $x_F > 0.1$ , we find  $Br(J/\psi \rightarrow \mu^+\mu^-) \cdot \sigma(\pi^- Be \rightarrow J/\psi + X)/A = (9.3 \pm 1.1(\text{sys}))$  nb/nucleon. The quoted error is dominated by systematic uncertainties in the luminosity, trigger and reconstruction efficiencies, and acceptance calculations. This result is consistent with our previous measurements [7,13,14].

For comparison with theory and with other experiments where the data cover different kinematic regions, we use the results of the fit to Eq. 4.1 to report the  $J/\psi$  cross section

for the region  $x_F > 0$ . This extrapolation requires a factor of  $1.39 \pm 0.05$ . The quoted error takes into account uncertainties in the  $x_F$  distribution at low  $x_F$ . The corresponding product of dimuon branching ratio and cross section is  $(12.9 \pm 1.6)$  nb/nucleon for  $x_F > 0$ . The dependence of the  $J/\psi$  cross section on  $\sqrt{s}$  for  $x_F > 0$  is shown in Fig. 10. The effect of the different target materials used by various experiments was accounted for by normalizing all data to beryllium assuming an  $A^{0.9}$  atomic mass dependence [1,7,15]. The curve in Fig. 10 represents a threshold production parameterization of the  $J/\psi$  cross section,

$$\sigma = \sigma_0(1 - M_{J/\psi}/\sqrt{s})^n, \quad (5.2)$$

with  $\sigma_0 = (25.6 \pm 1.8)$  nb/nucleon and  $n = 7.3 \pm 0.25$ .

## VI. $\psi(2S)$ PRODUCTION

We have detected  $\psi(2S)$  both in the dimuon (Fig. 4) and in the  $\psi(2S) \rightarrow J/\psi \pi^+ \pi^-$  (Fig. 11) decay modes. We report upon (i) differential and integrated  $\psi(2S)$  cross sections, (ii) the fraction of inclusive  $J/\psi$ s due to  $\psi(2S)$  decays, and (iii) the ratio of the  $\psi(2S)$  decay rates into  $J/\psi \pi^+ \pi^-$  and  $\mu^+ \mu^-$ .

For the analysis of  $J/\psi \pi^+ \pi^-$  final states we used the  $J/\psi$  candidate four-momenta combined with the four-momenta of two fully linked, opposite-sign charged tracks (assumed to be pions) originating from the same vertex as the  $J/\psi$ . The  $J/\psi \pi^+ \pi^-$  mass was calculated by adding the nominal  $J/\psi$  mass to the difference between the invariant masses of the  $\mu^+ \mu^- \pi^+ \pi^-$  and  $\mu^+ \mu^-$  systems. Tracks identified either as muons (penetrating through the muon detector) or as electrons from photon conversions (pairs of opposite charge particles with an invariant mass less than 20 MeV/ $c^2$ ) were not considered as candidate pion tracks. We also required the ratio of invariant masses,  $R_{\pi\pi} = M_{\pi\pi}/(M_{\mu\mu\pi\pi} - M_{\mu\mu})$ , to be greater than 0.8. This requirement was imposed since, according to Brown and Cahn [16], the phase space for a decay such as  $\psi(2S) \rightarrow J/\psi \pi^+ \pi^-$  is modified by chiral symmetry so that the di-pion mass distribution is skewed toward high values, a conjecture strongly supported by Mark III data [17]. Our data, shown in Fig. 12, are also consistent with this  $R_{\pi\pi}$

distribution. The requirement of  $R_{\pi\pi} > 0.8$  reduced combinations by a factor of 4 with an expected 23% loss of  $\psi(2S)$  signal.

The resulting  $J/\psi\pi^+\pi^-$  mass plot, shown in Fig. 11, exhibits a clear  $\psi(2S)$  signal with a FWHM of  $12 \text{ MeV}/c^2$  which is consistent with Monte Carlo simulation. A fit to the  $J/\psi\pi^+\pi^-$  mass spectrum using a two-gaussian resolution function for the signal and a fifth-order polynomial for background yields  $224 \pm 44(stat) \pm 20(sys)$  background-subtracted combinations. The  $\psi(2S)$  mass obtained from the fit is  $(3.684 \pm 0.002) \text{ GeV}/c^2$ . The systematic error in the number of  $\psi(2S)$  reflects the uncertainty in the background and signal shape.

The  $\psi(2S)$  differential cross sections as functions of  $x_F$  and  $p_T^2$  are shown in Fig. 13 and tabulated in Table 2. These distributions were obtained by fitting the  $J/\psi\pi^+\pi^-$  mass spectra in bins of  $x_F$  and  $p_T^2$ . The resulting background-subtracted signals in each bin were then corrected for acceptance and reconstruction efficiency including the effects of the  $R_{\pi\pi}$  requirement. They are normalized to the branching ratio times measured integrated cross section (discussed below). The only other measurements of the  $\psi(2S)$  differential distributions of which we are aware have been done in the dimuon mode using 150 GeV/c incident pions [18] and 800 GeV/c protons in the central  $x_F$  region [19,20].

The solid curves in Fig. 13 represent the parameterizations given by Eqs. 4.1-4.3 with the  $\psi(2S)$  mass substituted for the  $J/\psi$  mass and with values for  $a, \kappa, \beta, c$  from the fit to the  $J/\psi$  differential spectra as reported in Section IV. The agreement shows that the shapes of the measured  $J/\psi$  and  $\psi(2S)$  differential distributions can be described by similar parameterizations. We use these parameterizations in the evaluation of acceptance and efficiency for the following  $\psi(2S)$  analyses.

Based upon the observed  $224 \pm 44(stat) \pm 20(sys)$   $\psi(2S)$ s we obtain a  $\psi(2S)$  inclusive cross section of  $Br(\psi(2S) \rightarrow J/\psi\pi^+\pi^-) \cdot \sigma(\pi^- Be \rightarrow \psi(2S) + X)/A = (7.4 \pm 1.5(stat) \pm 1.2(sys))$  nb/nucleon for  $x_F > 0.1$ . The quoted systematic uncertainty assumes the  $J/\psi$  and  $\psi(2S)$   $x_F$  distributions have the same parameterization and takes into account variation in the measured  $J/\psi$   $x_F$  distribution (a variation of  $\pm 0.4$  in the value of  $\kappa = 2.2$  in Eq. 4.1). It does not account for possible contributions due to the  $R_{\pi\pi}$  requirement.

Using the branching ratios  $Br(J/\psi \rightarrow \mu^+\mu^-) = 0.0597 \pm 0.0025$  and  $Br(\psi(2S) \rightarrow J/\psi \pi^+\pi^-) = 0.324 \pm 0.026$  [10], the ratio of the inclusive cross sections,  $\sigma(\pi^- Be \rightarrow \psi(2S) + X)/\sigma(\pi^- Be \rightarrow J/\psi + X)$  is  $0.15 \pm 0.03(stat) \pm 0.02(sys)$ . This ratio is consistent with results obtained at lower energies, as shown in Fig. 14 and exhibits little dependence over the currently accessible  $\sqrt{s}$  range.

The contribution of all  $\psi(2S)$  decays to the observed  $J/\psi$  signal is given by

$$f_{\psi(2S)} = \frac{N'_{\psi(2S) \rightarrow J/\psi \pi^+ \pi^-} \cdot Br(\psi(2S) \rightarrow J/\psi X)}{N_{J/\psi \rightarrow \mu^+ \mu^-} \cdot Br(\psi(2S) \rightarrow J/\psi \pi^+ \pi^-)} \cdot k_1, \quad (6.1)$$

where  $Br(\psi(2S) \rightarrow J/\psi X) = 0.57 \pm 0.04$  [10].  $N_{J/\psi \rightarrow \mu^+ \mu^-} = 9600 \pm 105(stat) \pm 200(sys)$  is the number of  $J/\psi$ s having  $x_F$  in the range 0.1 to 0.8, and  $N'_{\psi(2S) \rightarrow J/\psi \pi^+ \pi^-} = 220 \pm 44(stat) \pm 20(sys)$  is the number of  $\psi(2S)$ s that decay into a  $J/\psi$  in the same  $x_F$  range.  $k_1$  is the relative detection efficiency (product of acceptance and reconstruction efficiency) of the  $J/\psi$  and  $\psi(2S)$  decay modes:

$$k_1 = \frac{a_{J/\psi \rightarrow \mu^+ \mu^-} \cdot \varepsilon_{J/\psi \rightarrow \mu^+ \mu^-}}{a_{\psi(2S) \rightarrow J/\psi \pi^+ \pi^-} \cdot \varepsilon_{\psi(2S) \rightarrow J/\psi \pi^+ \pi^-}} = 2.07 \pm 0.12(sys). \quad (6.2)$$

Using the above values, we find  $f_{\psi(2S)} = 0.083 \pm 0.017(stat) \pm 0.013(sys)$  in the  $J/\psi$   $x_F$  range 0.1 to 0.8. The quoted systematic uncertainty does not account for uncertainties due to the  $R_{\pi\pi}$  requirement. This is the first determination of  $f_{\psi(2S)}$  using a  $\psi(2S)$  decay mode into  $J/\psi$  as signal; previous measurements used the  $\mu^+\mu^-$  decay mode of the  $\psi(2S)$  [21–23]. Our value for  $f_{\psi(2S)}$  is consistent with these measurements.

The ratio of the  $\psi(2S)$  decay partial widths is determined as follows:

$$\frac{Br(\psi(2S) \rightarrow J/\psi \pi^+ \pi^-)}{Br(\psi(2S) \rightarrow \mu^+ \mu^-)} = \frac{N_{\psi(2S) \rightarrow J/\psi \pi^+ \pi^-}}{N_{\psi(2S) \rightarrow \mu^+ \mu^-} \cdot Br(J/\psi \rightarrow \mu^+ \mu^-)} \cdot k_2, \quad (6.3)$$

where  $N_{\psi(2S) \rightarrow J/\psi \pi^+ \pi^-} = 224 \pm 44(stat) \pm 20(sys)$  and  $N_{\psi(2S) \rightarrow \mu^+ \mu^-} = 270 \pm 35(stat) \pm 50(sys)$ , and  $k_2 = 2.17 \pm 0.17(sys)$  is the ratio of the detection efficiencies between the two modes. We find  $Br(\psi(2S) \rightarrow J/\psi \pi^+ \pi^-)/Br(\psi(2S) \rightarrow \mu^+ \mu^-) = 30.2 \pm 7.1(stat) \pm 6.8(sys)$  (again, the quoted systematic uncertainty does not include contributions due to the  $R_{\pi\pi}$  requirement). The current world average for this ratio calculated from Particle Data Group information is  $42 \pm 10$  [10].

## VII. SEARCH FOR “HIDDEN” CHARM RESONANCE STATES

We searched for evidence of the enhancement in the  $J/\psi\pi^+\pi^-$  mass spectrum around  $3.836 \text{ GeV}/c^2$  reported in ref. [24]. A fit to the mass spectrum obtained in the  $\psi(2S)$  analysis (see Section VI) was performed using a double gaussian resolution function centered at  $3.836 \text{ GeV}/c^2$  for the “hidden” charm candidate in addition to the  $\psi(2S)$  and background shapes. Figure 14a shows the result of this fit. The excess was calculated as the number of entries above the resultant fitted background in the mass region  $(3.836 \pm 0.015) \text{ GeV}/c^2$ . This procedure yields  $52 \pm 30(stat)$  background-subtracted combinations to be compared with  $224 \pm 44 \psi(2S)$  events. This leads to a  $3.1 \text{ nb/nucleon}$  upper limit (90% confidence level) on the value for  $Br(X(3836) \rightarrow J/\psi\pi^+\pi^-) \cdot \sigma(\pi^- Be \rightarrow X(3836) + X)/A$  for  $x_F > 0.1$  assuming the same production properties for the  $\psi(2S)$  and the “hidden” charm resonance. The 90% confidence level upper limit is the cross section calculated for the (statistically insignificant) number of background-subtracted combinations observed plus 1.28 times the sum (in quadrature) of the statistical and 20% systematic uncertainties.

We have also investigated  $J/\psi\pi^\pm$  and  $\psi(2S)\pi^\pm$  spectra in a search for charged resonance states decaying into either  $J/\psi$  or  $\psi(2S)$  plus a single charged pion. The  $\psi(2S) \rightarrow J/\psi\pi^+\pi^-$  events were used in this search. As shown in Figs. 14b and 14c, the data indicate no evidence for significant structure. Mass spectra obtained by combining  $J/\psi$  or  $\psi(2S)$  and pions from different events are also shown for comparison.

## VIII. SUMMARY

We have studied the production of the  $J/\psi$  and  $\psi(2S)$  charmonium mesons in  $515 \text{ GeV}/c$   $\pi^- Be$  collisions in the Feynman- $x$  range  $0.1 < x_F < 0.8$ . For  $x_F > 0.1$  we measure cross sections of  $Br(J/\psi \rightarrow \mu^+\mu^-) \cdot \sigma(\pi^- Be \rightarrow J/\psi + X)/A = (9.3 \pm 1.1(sys)) \text{ nb/nucleon}$  and  $Br(\psi(2S) \rightarrow J/\psi\pi^+\pi^-) \cdot \sigma(\pi^- Be \rightarrow \psi(2S) + X)/A = (7.4 \pm 1.5(stat) \pm 1.2(sys)) \text{ nb/nucleon}$ . The shapes of the measured differential distributions for the  $J/\psi$  and  $\psi(2S)$



can be adequately described by the same parameterization.

The fraction of the inclusive  $J/\psi$  yield due to  $\psi(2S)$  decays is  $f_{\psi(2S)} = 0.083 \pm 0.017(stat) \pm 0.013(sys)$ . The ratio of two  $\psi(2S)$  decay rates  $Br(\psi(2S) \rightarrow J/\psi \pi^+ \pi^-) / Br(\psi(2S) \rightarrow \mu^+ \mu^-)$  is  $30.2 \pm 7.1(stat) \pm 6.8(sys)$ .

We have also searched for production of “hidden” charm resonances decaying into either  $J/\psi \pi^\pm$ ,  $\psi(2S) \pi^\pm$  or  $J/\psi \pi^+ \pi^-$  systems. We find no statistically significant evidence for the recently observed enhancement at a  $J/\psi \pi^+ \pi^-$  mass of  $3.836 \text{ GeV}/c^2$ .

We thank the staffs of all the participating institutions, especially those of Fermilab and the Institute for High Energy Physics (IHEP) at Protvino. This work was supported by the U.S. Department of Energy, the National Science Foundation, and the Russian Ministries of Science and Atomic Energy.

## REFERENCES

- [1] G. A. Schuler, “Quarkonium Production and Decays”, CERN-TH.7170/94 (1994).
- [2] M. Vanttinen, P. Hoyer, S. J. Brodsky, and W. -K. Tang, Phys. Rev. **D51**, 3332 (1995).
- [3] V. Koreshev *et al.*, “Production of Charmonium States in  $\pi^-$  Be Collisions at 515 GeV/ $c$ ”, in preparation.
- [4] E. Engels, Jr. *et al.*, Nucl. Instr. & Meth. **A279**, 272 (1989).
- [5] C. Bromberg *et al.*, Nucl. Instr. & Meth. **A307**, 292 (1991).
- [6] F. Lobkowicz *et al.*, Nucl. Instr. & Meth. **A235**, 332 (1985); G. Alverson *et al.*, Phys. Rev. **D48**, 5 (1993).
- [7] S. Kartik *et al.*, Phys. Rev. **D41**, 1 (1990).
- [8] V. Abramov *et al.*, “Properties of  $J/\psi$  Production in  $\pi^-$  Be and p-Be Collisions at 530 GeV/ $c$ ”, FERMILAB-Pub-91/62-E (1991).
- [9] R. R. Crittenden *et al.*, Nucl. Instr. & Meth. **A270**, 99 (1988).
- [10] Particle Data Group, Phys. Rev. **D50**, 1173 (1994).
- [11] V. G. Kartvelishvili and A. K. Likhoded, Sov. J. Nucl. Phys. **39**, 298 (1984).
- [12] D. M. Kaplan *et al.*, Phys. Rev. Lett. **40**, 435 (1978).
- [13] Cross sections quoted in preprint ref. [8] must be increased by a factor 1.2 to account for an omitted correction in the luminosity calculations.
- [14] Note that the measurement reported in R. Jesik *et al.*, Phys. Rev. Lett. **74**, 495 (1995) is not independent since it is based upon an analysis of the data from the sample discussed in this paper.
- [15] D. M. Alde *et al.*, Phys. Rev. Lett. **66**, 133 (1991).

- [16] L. S. Brown and R. N. Cahn, Phys. Rev. Lett. **35**, 1 (1975).
- [17] D. Coffman *et al.*, Phys. Rev. Lett. **68**, 282 (1992).
- [18] M. A. Abolins *et al.*, Phys. Lett. **82B**, 145 (1979).
- [19] T. Alexopoulos *et al.*, “Production of  $J/\psi$  in 800 GeV/ $c$  p Si Interactions”, FERMILAB Conf-94/178-E (1994).
- [20] M. H. Schub *et al.*, “Measurement of  $J/\psi$  and  $\psi'$  in 800 GeV/ $c$  Proton-Gold Collisions”, FERMILAB Pub-95/058-E (1995), submitted to Phys. Rev. D.
- [21] J.G. McEwen *et al.*, Phys. Lett. **121B**, 198 (1983).
- [22] S. R. Hahn *et al.*, Phys. Rev. **D30**, 671 (1984).
- [23] L. Antoniazzi *et al.*, Phys. Rev. Lett. **70**, 383 (1993).
- [24] L. Antoniazzi *et al.*, Phys. Rev. **D50**, 4258 (1994).
- [25] J. Alspector *et al.*, Phys. Lett. **81B**, 397 (1979); J. LeBritton *et al.*, Phys. Lett. **81B**, 401 (1979).
- [26] Yu. B. Bushnin *et al.*, Phys. Lett. **72B**, 269 (1977).
- [27] F. Binon *et al.*, Nucl. Phys. **B239**, 311 (1984).
- [28] M. J. Corden *et al.*, Phys. Lett. **68B**, 96 (1977); Phys. Lett. **96B**, 411 (1980).
- [29] Yu. M. Antipov *et al.*, Phys. Lett. **72B**, 278 (1977);
- [30] S. Katsanevas *et al.*, Phys. Rev. Lett. **60**, 2121 (1988); C. Akerlof *et al.*, Phys. Rev. **D48**, 5067 (1993).
- [31] J. Badier *et al.*, Z. Phys. **C20**, 101 (1983).
- [32] J. G. Branson *et al.*, Phys. Rev. Lett. **38**, 1331 (1977).
- [33] K. J. Anderson *et al.*, Phys. Rev. Lett. **42**, 944 (1979).

[34] L. Antoniazzi *et al.*, Phys. Rev. **D46**, 4828 (1992).

# FIGURES

Table 1. Differential cross sections for  $J/\psi$  production.

$x_F$ bin	$d\sigma/dx_F$ nb/nucleon	$p_T^2$ bin (GeV/c) <sup>2</sup>	$d\sigma/dp_T^2$ nb/nucleon/(GeV/c) <sup>2</sup>	$\cos\theta$ bin	$d\sigma/d\cos\theta$ nb/nucleon
		0.0–0.2	$6.39 \pm 0.17$		
		0.2–0.4	$4.82 \pm 0.15$		
		0.4–0.6	$4.48 \pm 0.14$		
		0.6–0.8	$3.60 \pm 0.13$		
		0.8–1.0	$3.10 \pm 0.12$		
0.10–0.12	$36.4 \pm 2.4$	1.0–1.2	$2.59 \pm 0.11$	–0.80—0.68	$4.71 \pm 0.37$
0.12–0.14	$31.3 \pm 1.8$	1.2–1.4	$2.29 \pm 0.10$	–0.68—0.64	$4.47 \pm 0.47$
0.14–0.16	$32.8 \pm 1.6$	1.4–1.6	$2.13 \pm 0.10$	–0.64—0.60	$3.89 \pm 0.37$
0.16–0.18	$32.3 \pm 1.4$	1.6–1.8	$1.706 \pm 0.089$	–0.60—0.56	$4.67 \pm 0.35$
0.18–0.20	$29.4 \pm 1.2$	1.8–2.0	$1.475 \pm 0.083$	–0.56—0.52	$4.74 \pm 0.32$
0.20–0.22	$26.9 \pm 1.1$	2.0–2.2	$1.246 \pm 0.077$	–0.52—0.48	$4.82 \pm 0.30$
0.22–0.24	$24.8 \pm 1.0$	2.2–2.4	$1.338 \pm 0.080$	–0.48—0.44	$4.92 \pm 0.28$
0.24–0.26	$26.6 \pm 1.0$	2.4–2.6	$1.048 \pm 0.071$	–0.44—0.40	$4.60 \pm 0.26$
0.26–0.28	$22.15 \pm 0.90$	2.6–2.8	$0.823 \pm 0.063$	–0.40—0.36	$4.79 \pm 0.25$
0.28–0.30	$19.07 \pm 0.82$	2.8–3.0	$0.947 \pm 0.068$	–0.36—0.32	$5.38 \pm 0.26$
0.30–0.32	$19.04 \pm 0.82$	3.0–3.2	$0.937 \pm 0.067$	–0.32—0.28	$4.84 \pm 0.24$
0.32–0.34	$16.40 \pm 0.75$	3.2–3.4	$0.634 \pm 0.056$	–0.28—0.24	$4.55 \pm 0.23$
0.34–0.36	$16.16 \pm 0.75$	3.4–3.6	$0.632 \pm 0.056$	–0.24—0.20	$4.57 \pm 0.23$
0.36–0.38	$14.53 \pm 0.71$	3.6–3.8	$0.639 \pm 0.056$	–0.20—0.16	$4.50 \pm 0.22$
0.38–0.40	$13.35 \pm 0.68$	3.8–4.0	$0.543 \pm 0.052$	–0.16—0.12	$4.69 \pm 0.23$
0.40–0.42	$12.26 \pm 0.66$	4.0–4.2	$0.456 \pm 0.048$	–0.12—0.08	$4.40 \pm 0.22$
0.42–0.44	$11.83 \pm 0.65$	4.2–4.4	$0.418 \pm 0.046$	–0.08—0.04	$4.81 \pm 0.23$
0.44–0.46	$10.42 \pm 0.61$	4.4–4.6	$0.414 \pm 0.045$	–0.04–0.00	$4.65 \pm 0.23$
0.46–0.48	$8.64 \pm 0.56$	4.6–4.8	$0.375 \pm 0.043$	0.00–0.04	$4.65 \pm 0.23$
0.48–0.50	$7.76 \pm 0.54$	4.8–5.0	$0.341 \pm 0.041$	0.04–0.08	$4.40 \pm 0.23$
0.50–0.52	$7.43 \pm 0.54$	5.0–5.2	$0.297 \pm 0.039$	0.08–0.12	$4.45 \pm 0.23$
0.52–0.54	$7.07 \pm 0.53$	5.2–5.4	$0.237 \pm 0.035$	0.12–0.16	$4.75 \pm 0.25$
0.54–0.56	$5.70 \pm 0.49$	5.4–5.6	$0.268 \pm 0.037$	0.16–0.20	$4.38 \pm 0.24$
0.56–0.58	$5.20 \pm 0.48$	5.6–5.8	$0.213 \pm 0.033$	0.20–0.24	$4.67 \pm 0.26$
0.58–0.60	$4.56 \pm 0.46$	5.8–6.0	$0.183 \pm 0.030$	0.24–0.28	$4.27 \pm 0.25$
0.60–0.62	$4.13 \pm 0.45$	6.0–6.2	$0.153 \pm 0.028$	0.28–0.32	$4.72 \pm 0.28$
0.62–0.64	$3.81 \pm 0.45$	6.2–6.4	$0.173 \pm 0.030$	0.32–0.36	$4.51 \pm 0.2$
0.64–0.66	$3.74 \pm 0.46$	6.4–6.6	$0.128 \pm 0.026$	0.36–0.40	$4.79 \pm 0.30$
0.66–0.68	$2.06 \pm 0.35$	6.6–6.8	$0.194 \pm 0.032$	0.40–0.44	$4.52 \pm 0.31$
0.68–0.70	$1.93 \pm 0.35$	6.8–7.0	$0.143 \pm 0.027$	0.44–0.48	$5.14 \pm 0.35$
0.70–0.72	$2.42 \pm 0.40$	7.0–7.2	$0.113 \pm 0.024$	0.48–0.52	$4.10 \pm 0.34$
0.72–0.74	$1.81 \pm 0.35$	7.2–7.4	$0.133 \pm 0.026$	0.52–0.56	$4.34 \pm 0.38$
0.74–0.76	$1.13 \pm 0.29$	7.4–7.6	$0.087 \pm 0.021$	0.56–0.60	$5.06 \pm 0.45$
0.76–0.78	$1.26 \pm 0.32$	7.6–7.8	$0.118 \pm 0.025$	0.60–0.64	$4.14 \pm 0.45$
0.78–0.80	$0.84 \pm 0.28$	7.8–8.0	$0.087 \pm 0.021$	0.64–0.68	$3.97 \pm 0.51$
		8.0–8.2	$0.113 \pm 0.024$	0.68–0.80	$5.25 \pm 0.79$
		8.2–8.4	$0.072 \pm 0.019$		
		8.4–8.6	$0.051 \pm 0.016$		
		8.6–8.8	$0.062 \pm 0.018$		
		8.8–9.0	$0.077 \pm 0.020$		
		9.0–9.2	$0.036 \pm 0.014$		
		9.2–9.4	$0.061 \pm 0.018$		
		9.4–9.6	$0.051 \pm 0.016$		
		9.6–9.8	$0.026 \pm 0.011$		
		9.8–10.0	$0.041 \pm 0.014$		

Table 2. Differential cross sections for  $\psi(2S)$  production

$x_F$ bin	$d\sigma/dx_F$ <i>nb/nucleon</i>	$p_T^2$ bin $(GeV/c)^2$	$d\sigma/dp_T^2$ <i>nb/nucleon/(GeV/c)<sup>2</sup></i>
		0.0 – 0.5	$4.2 \pm 1.4$
0.10–0.24	$23.1 \pm 9.3$	0.5 – 1.0	$3.8 \pm 1.4$
0.24–0.38	$13.9 \pm 4.4$	1.0 – 1.5	$3.2 \pm 1.2$
0.38–0.52	$8.8 \pm 3.2$	1.5 – 2.0	$2.4 \pm 1.3$
0.52–0.66	$5.6 \pm 2.1$	2.0 – 2.5	$0.4 \pm 1.2$
0.66–0.80	$1.4 \pm 1.0$	2.5 – 3.0	$0.8 \pm 1.0$

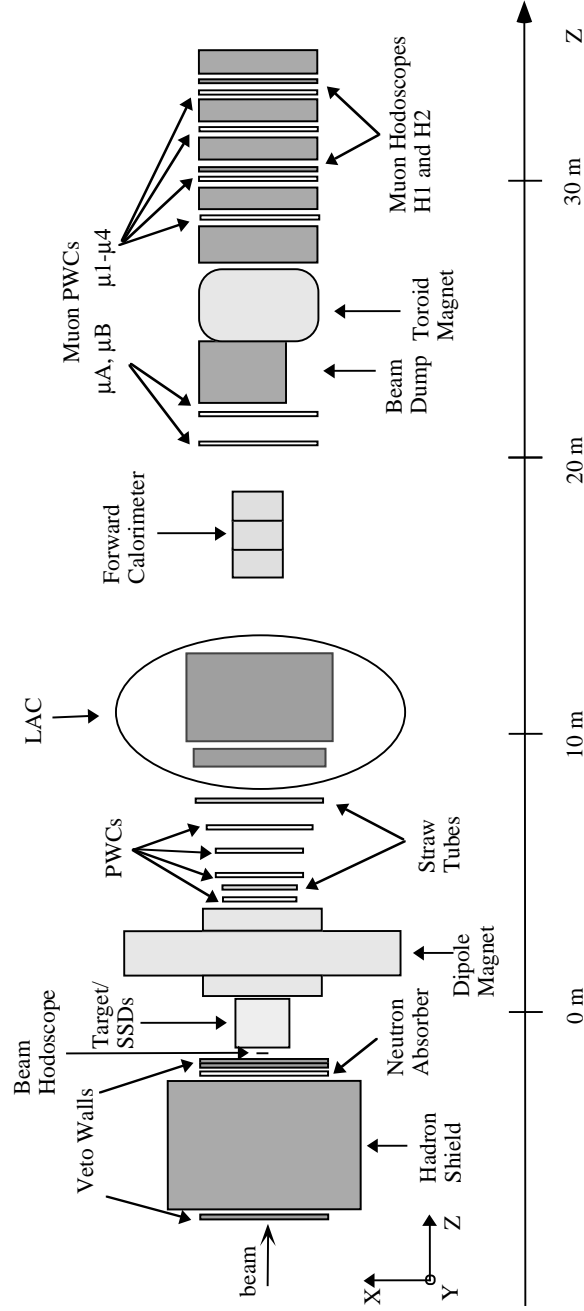


FIG. 1. Plan view of the Fermilab Meson West spectrometer during the 1990 run.

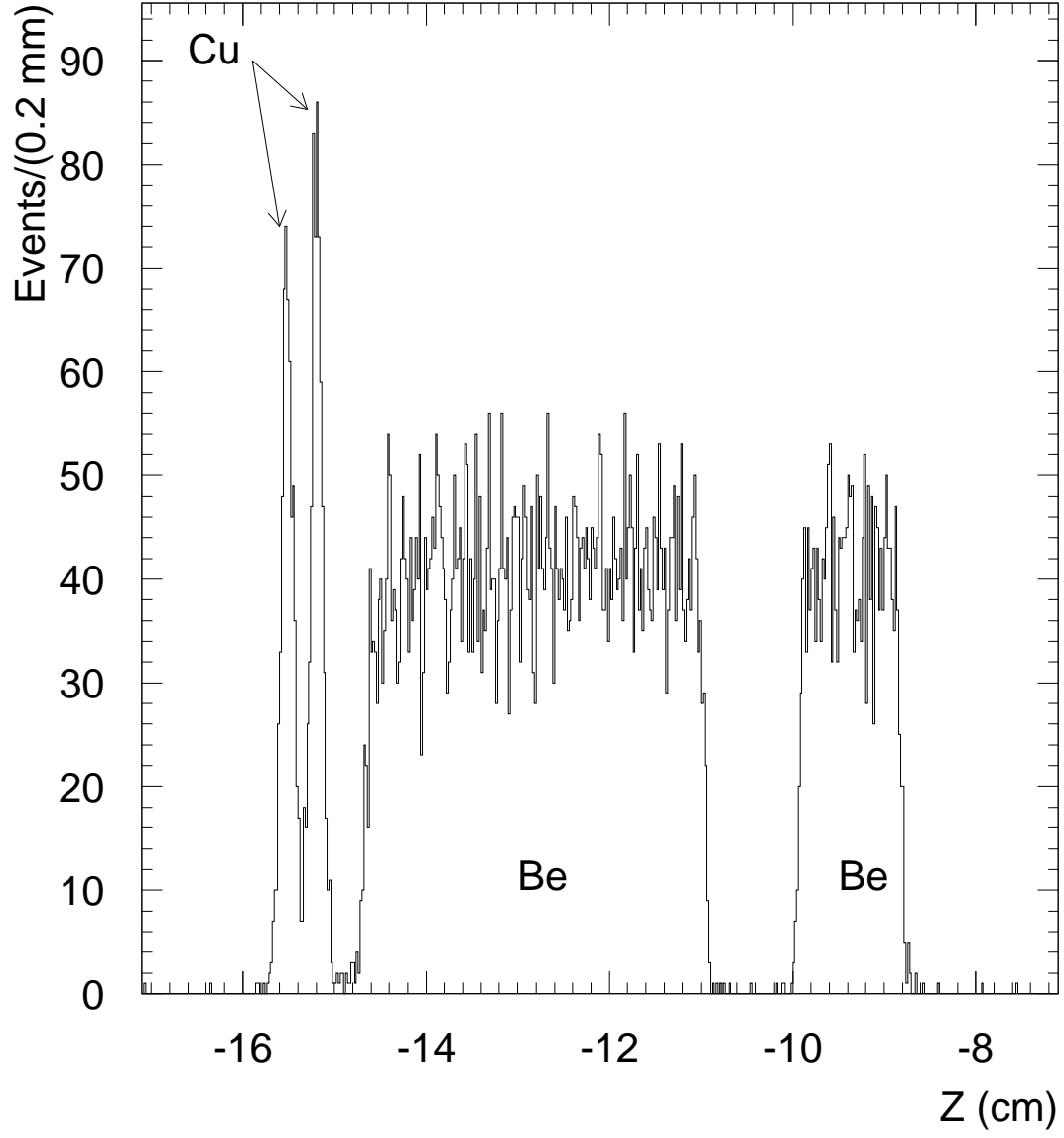


FIG. 2. Primary vertex Z-coordinate distribution for events containing reconstructed  $J/\psi$ s.



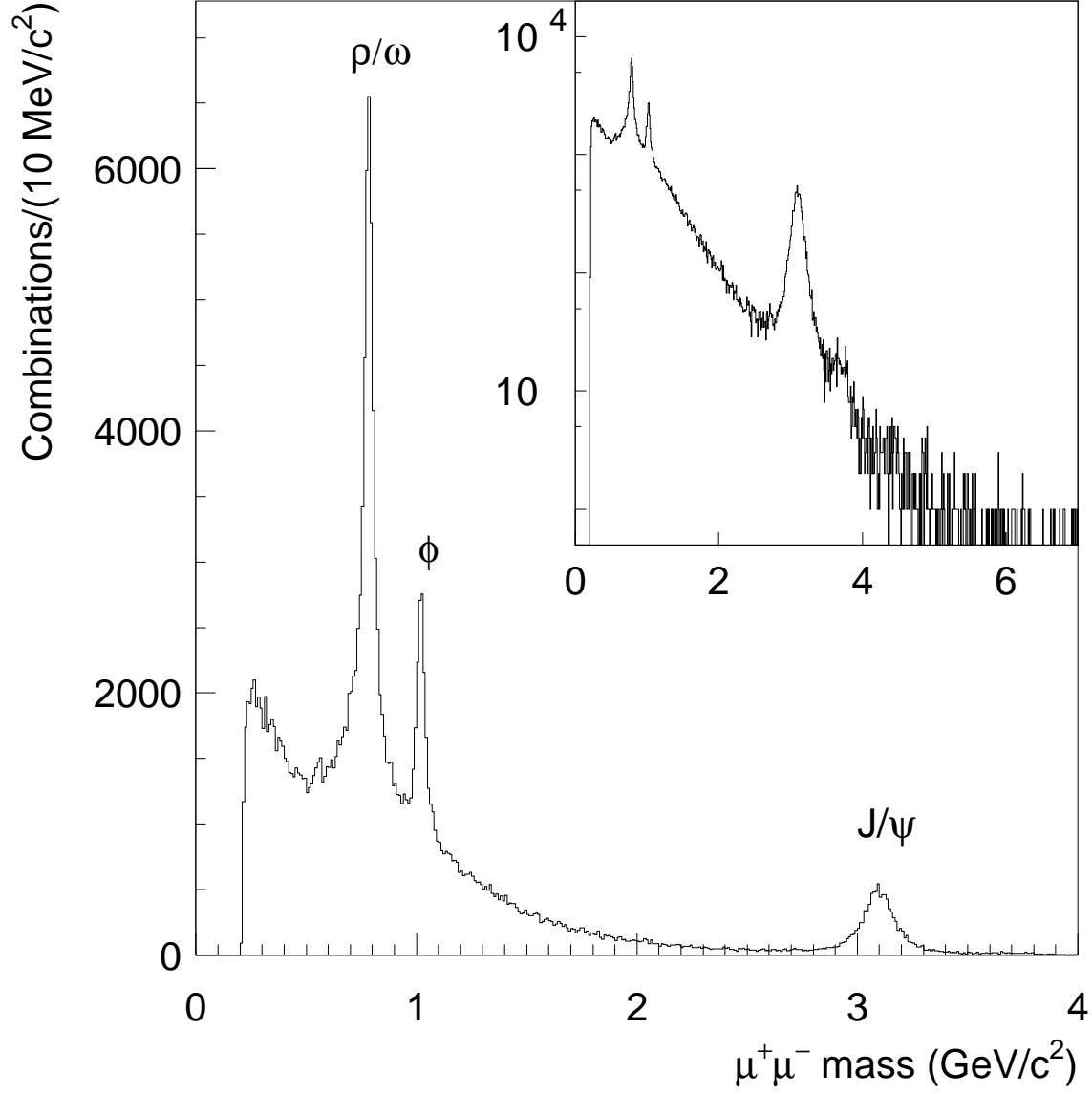


FIG. 3. The invariant mass distribution of  $\mu^+\mu^-$  pairs produced by  $\pi^-Be$  interactions (data were collected with varying dimuon trigger processor mass thresholds). The inset displays the data in a semi-log format.

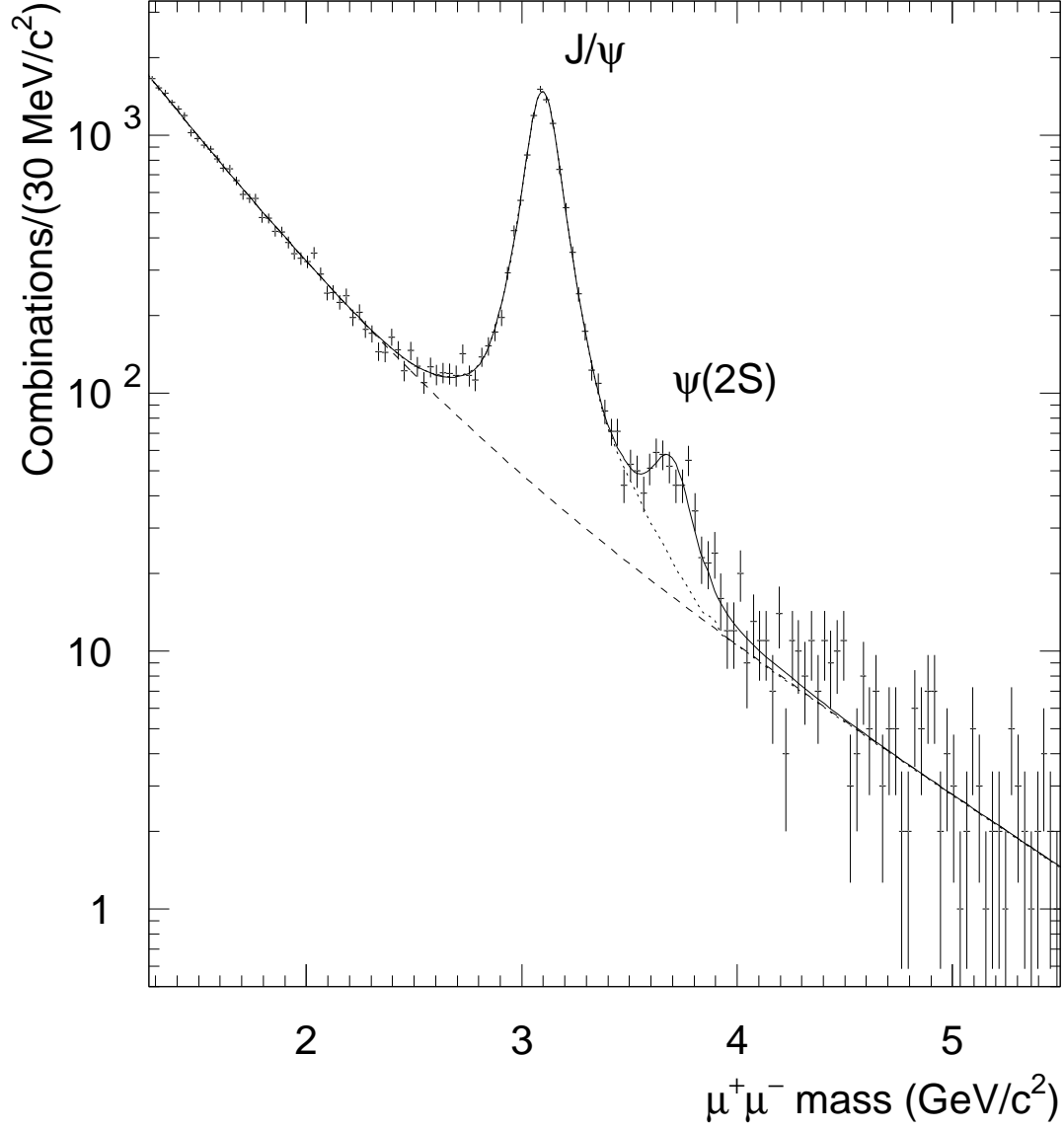


FIG. 4. The invariant mass distribution for  $\mu^+\mu^-$  pairs in the  $J/\psi$  mass region. The solid curve is a fit to the data; the dashed curve shows the background contribution, and the dotted curve illustrates the background under the  $\psi(2S)$  signal.

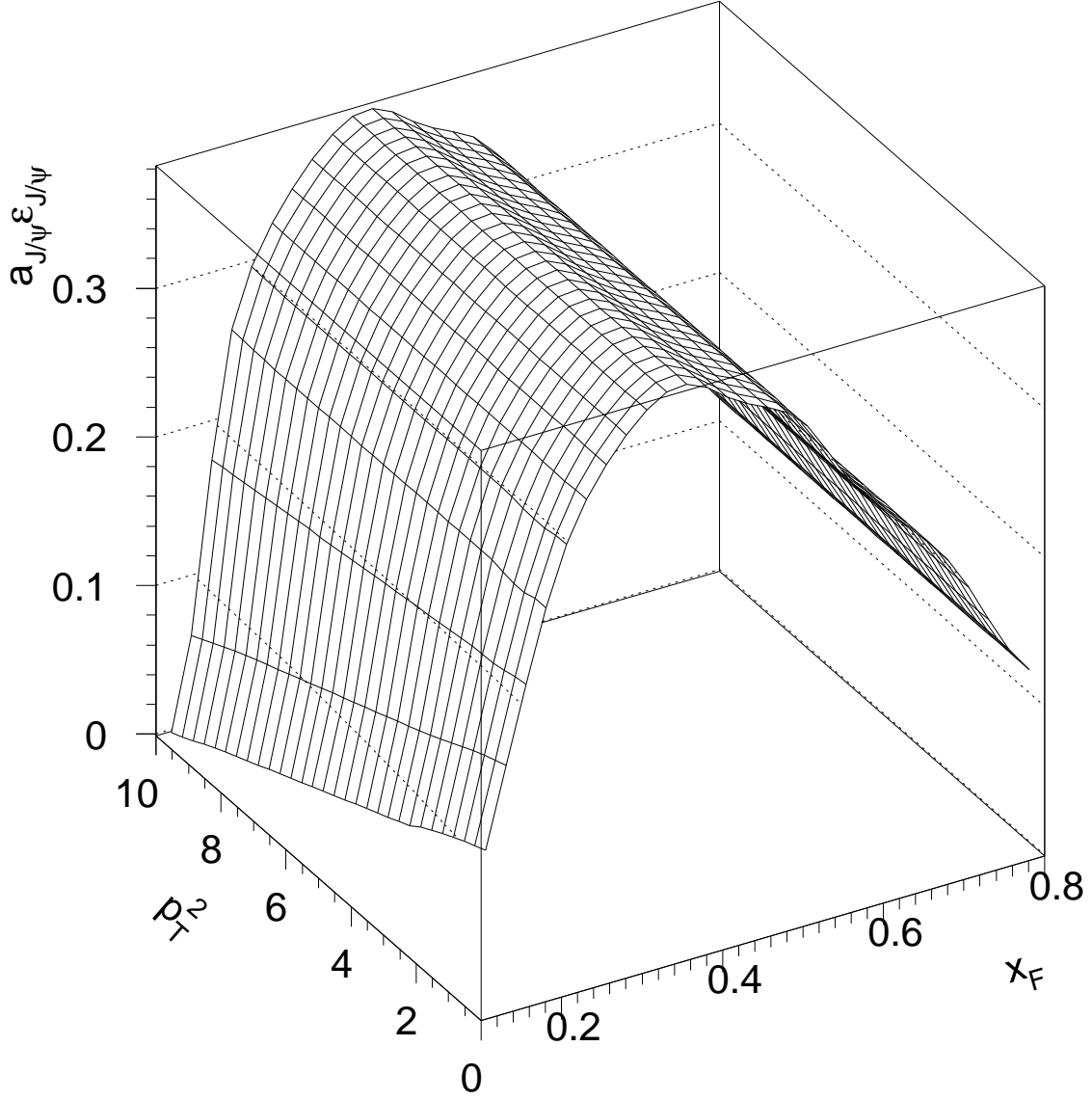


FIG. 5. Surface illustrating the product of geometrical acceptance and reconstruction efficiency for the  $J/\psi \rightarrow \mu^+ \mu^-$  decay as a function of  $x_F$  and  $p_T^2$ .

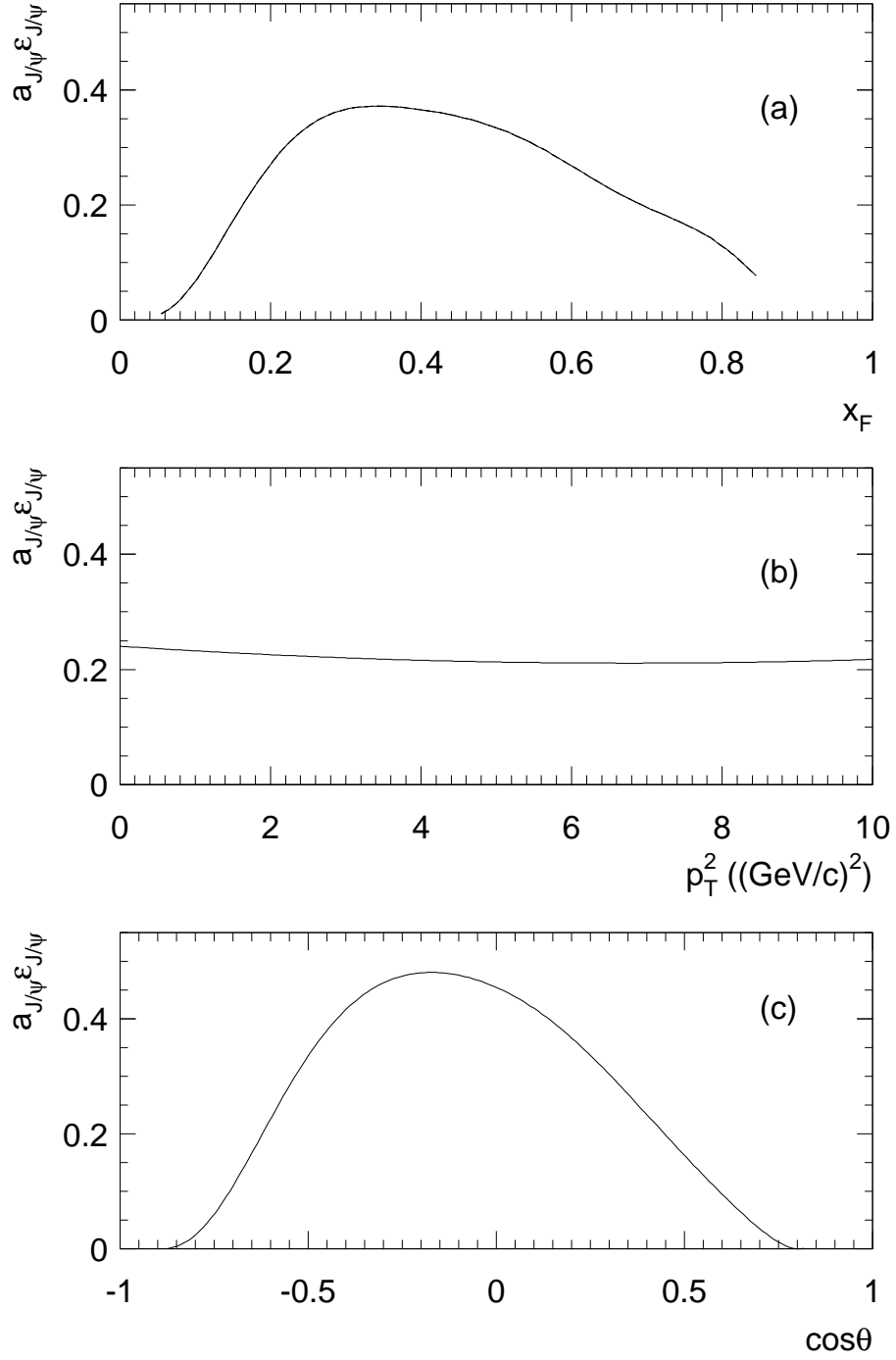


FIG. 6. Product of geometrical acceptance and reconstruction efficiency for the  $J/\psi \rightarrow \mu^+ \mu^-$  decay as a function of: (a)  $x_F$ , (b)  $p_T^2$ , and (c)  $\cos \theta$ .

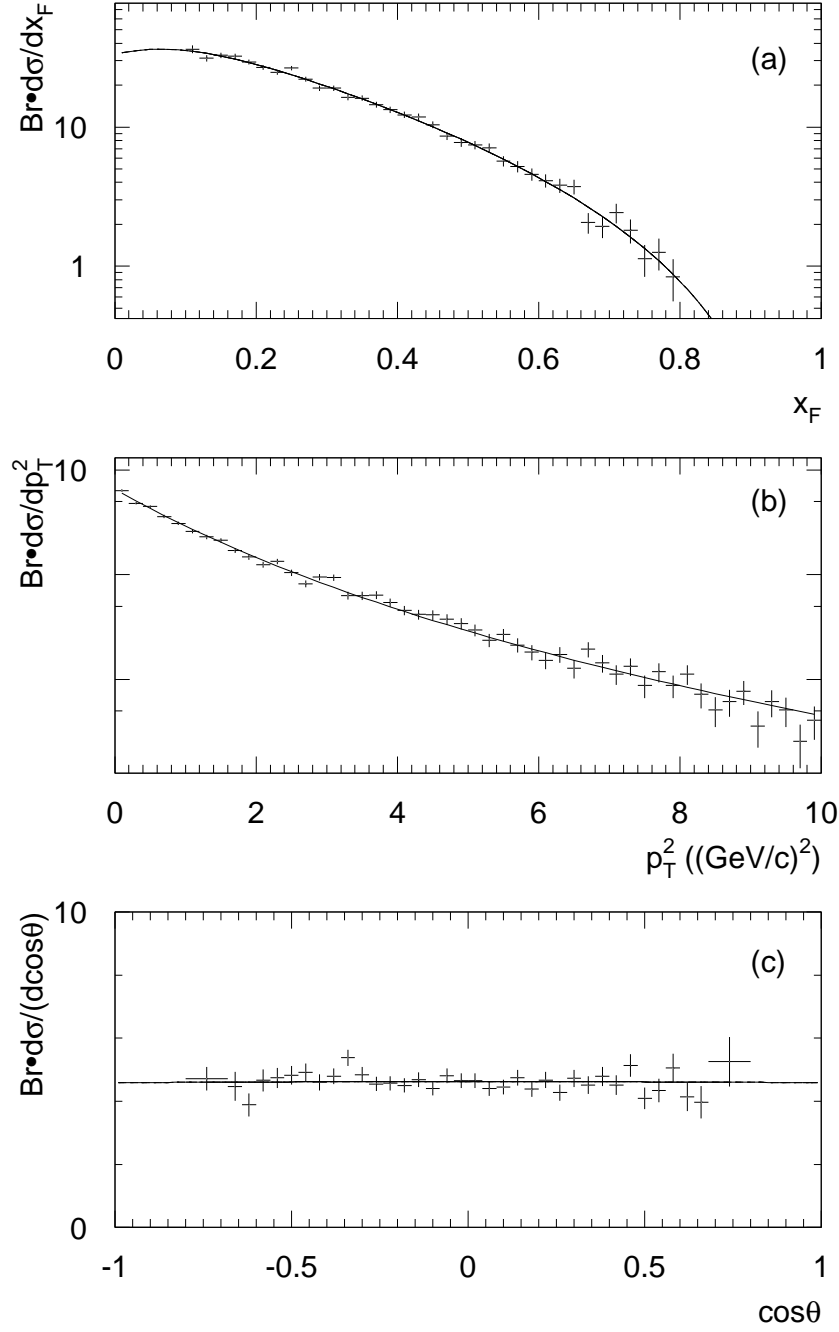


FIG. 7. Product of  $Br(J/\psi \rightarrow \mu^+\mu^-)$  and  $J/\psi$  differential cross section as a function of: (a)  $x_F$  (nb/nucleon), (b)  $p_T^2$  (nb/nucleon/ $(\text{GeV}/c)^2$ ), and (c)  $\cos\theta$  (nb/nucleon). Solid curves representing empirical fits to the data are described in the text (uncertainties are statistical only; the overall normalization uncertainty is  $\pm 12\%$ ).

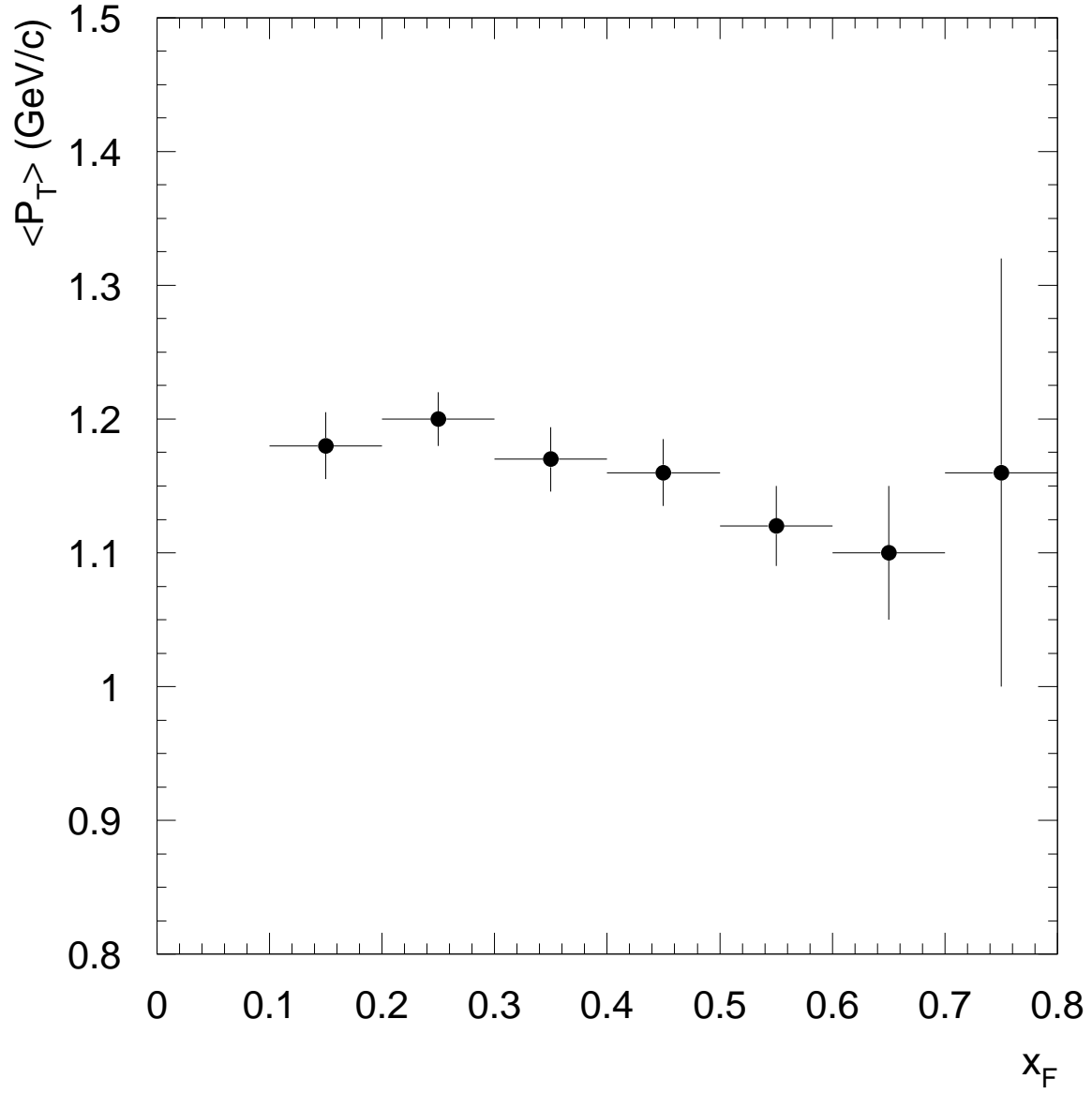


FIG. 8. The average  $J/\psi$  transverse momentum,  $\langle p_T \rangle$  vs the  $J/\psi$   $x_F$  (uncertainties are statistical only).

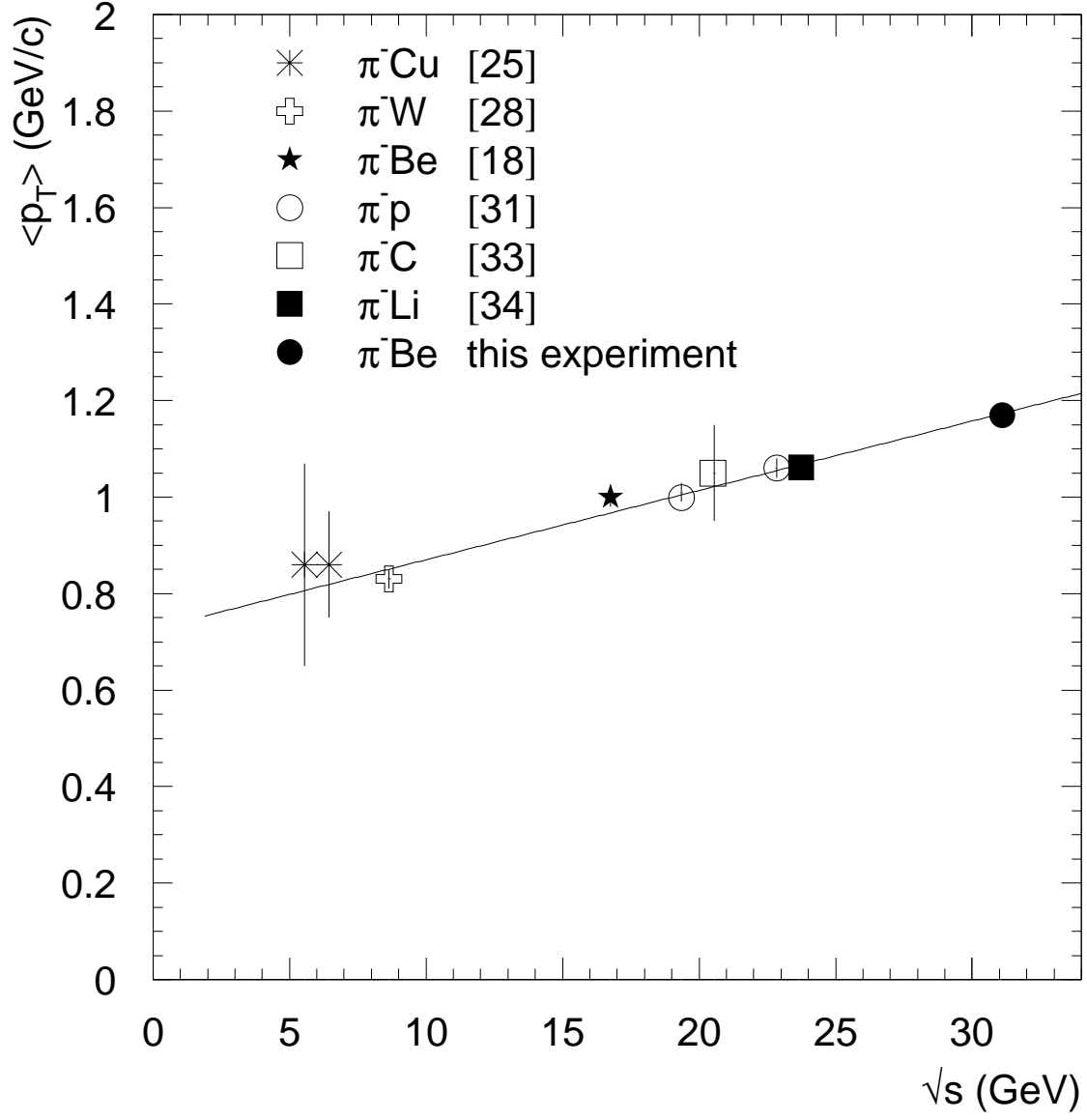


FIG. 9. Dependence of  $\langle p_T \rangle$  of  $J/\psi$  on  $\sqrt{s}$  for  $\pi^-$ -nucleon interactions. The data are fitted with a linear function (uncertainties are statistical and systematic added in quadrature).

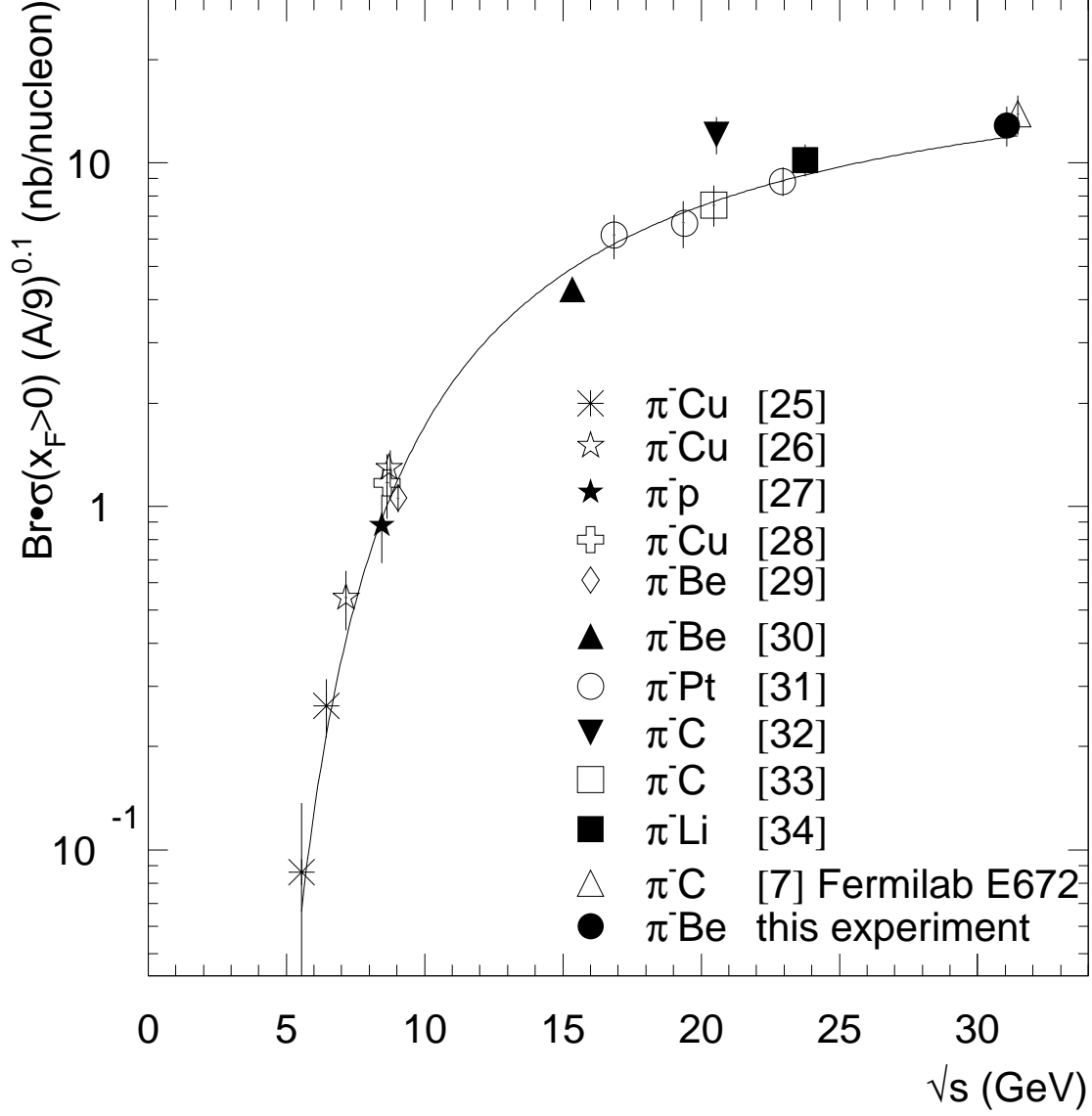


FIG. 10. Dependence of the product  $Br \cdot \sigma_{J/\psi}$  for  $x_F > 0$  on  $\sqrt{s}$  for  $\pi^-$ -nucleon interactions (uncertainties are statistical and systematic added in quadrature). Measurements from different targets have been normalized to Be assuming an  $A^{0.9}$  atomic mass dependence. The curve represents the threshold production parameterization described in the text. Results from previous experiments have been adjusted to account for the appropriate  $J/\psi \rightarrow \mu^+ \mu^-$  branching ratio when necessary.



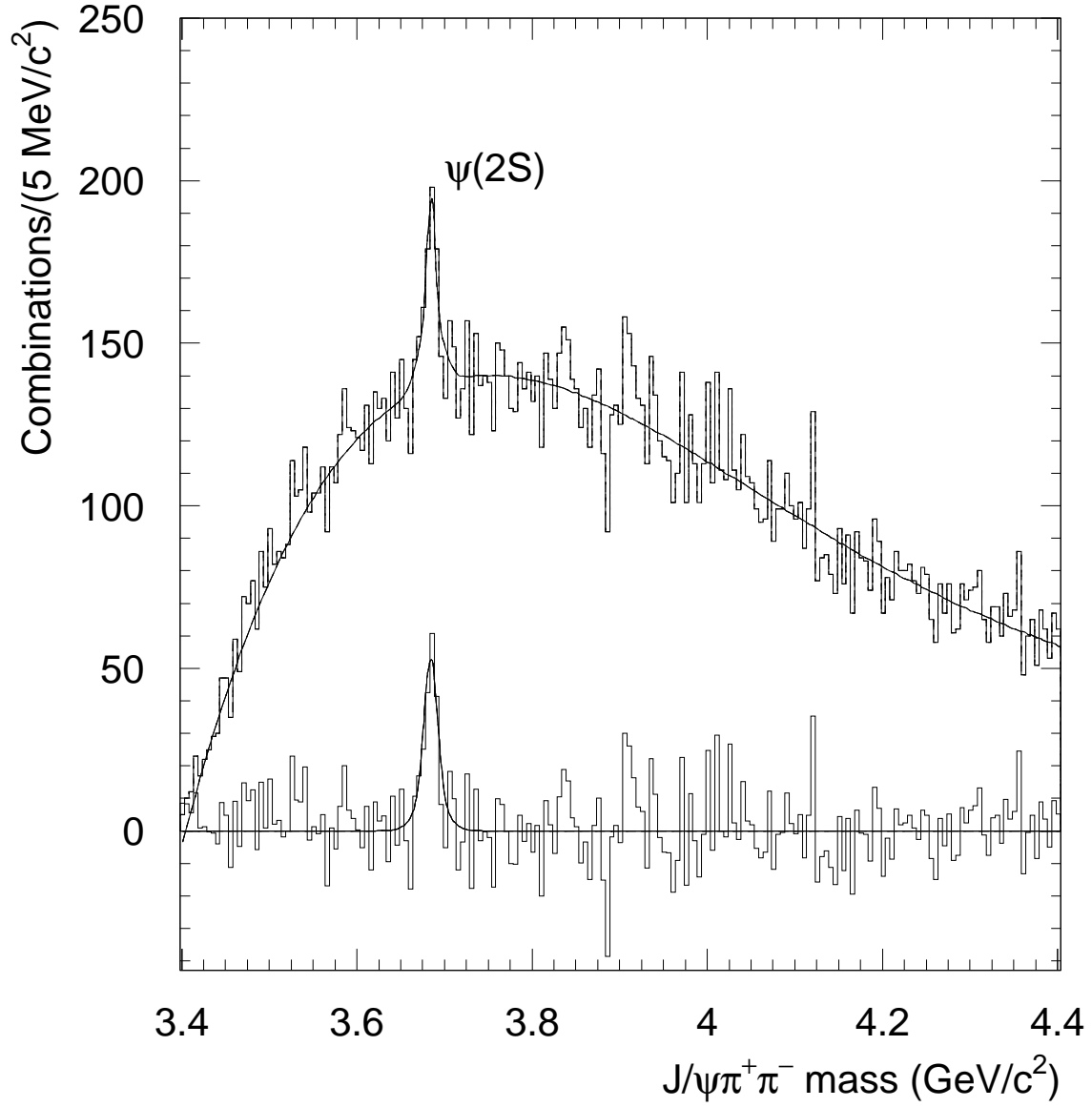


FIG. 11. The  $J/\psi\pi^+\pi^-$  invariant mass distribution. The solid curve shows the fit to the data described in the text. The lower histogram shows the background-subtracted signal with Monte Carlo expectation superimposed (solid curve).

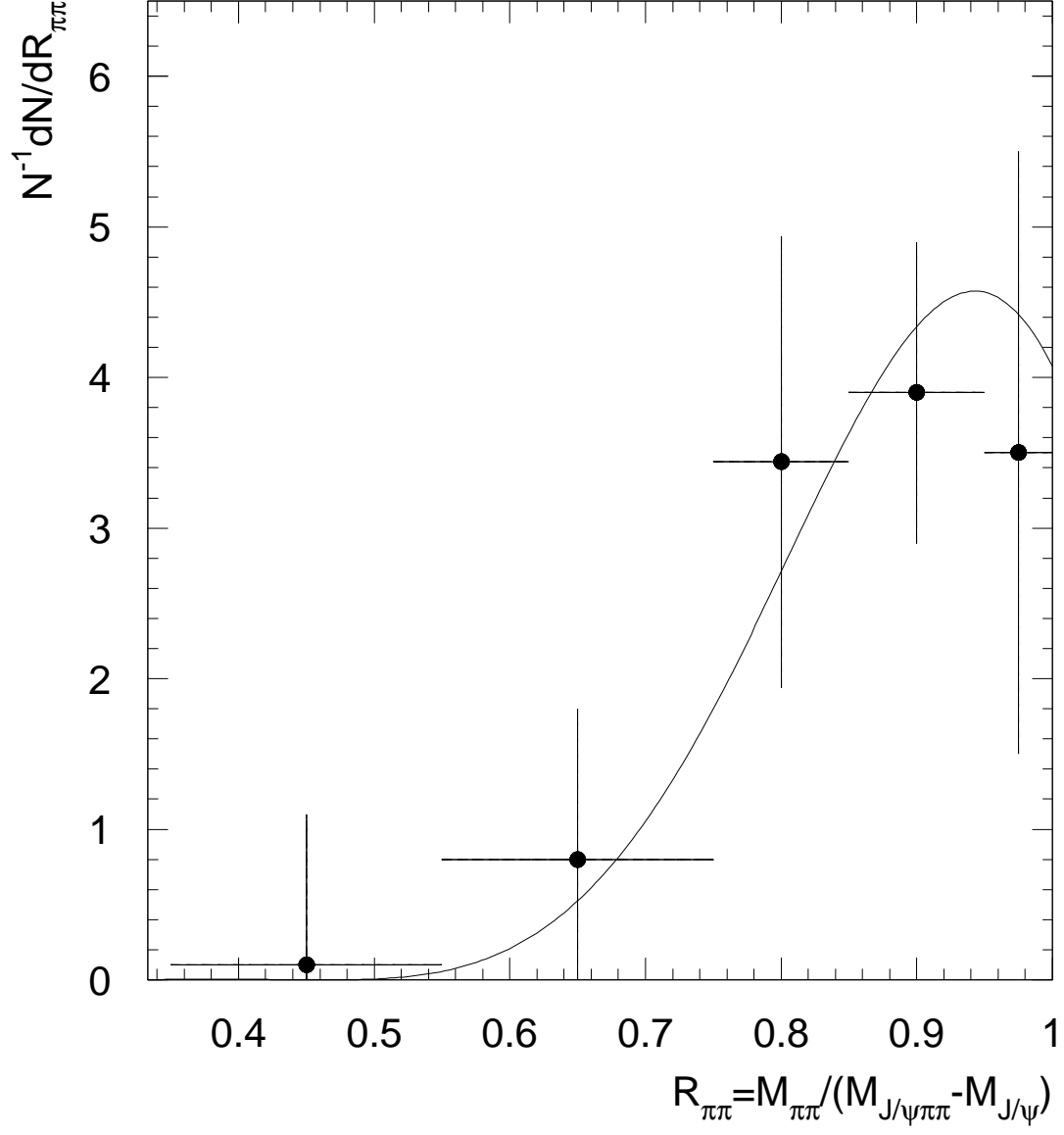


FIG. 12. The distribution of  $R_{\pi\pi}$  for  $\psi(2S) \rightarrow J/\psi \pi^+ \pi^-$  decays. The points represent our data after background subtraction; the curve represents a parameterization of the Mark III results [17].

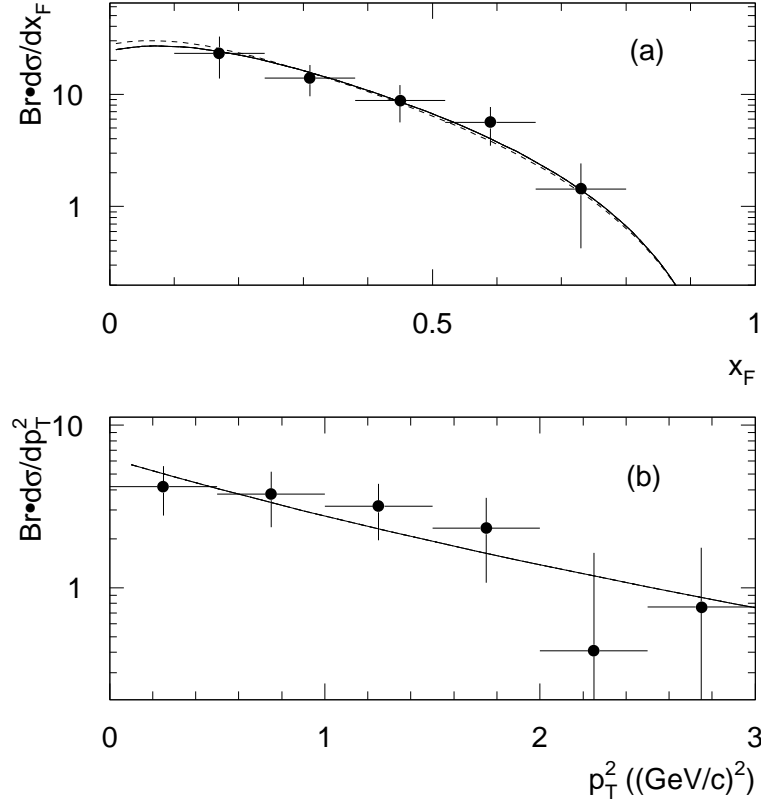


FIG. 13. Product of  $Br(\psi(2S) \rightarrow J/\psi \pi^+ \pi^-)$  and  $\psi(2S)$  differential cross section as a function of: (a)  $x_F$  (nb/nucleon), (b)  $p_T^2$  (nb/nucleon/ $(\text{GeV}/c)^2$ ). The solid curves are the parameterizations given by Eqs. 4.1-4.3 using the values of the parameters determined by the fits for  $J/\psi$  production and substituting the  $\psi(2S)$  mass in the  $\tau$  calculation. The shape of the fitted inclusive  $J/\psi$   $x_F$  distribution is shown as a dashed curve in (a) for comparison. The curves are normalized to the  $\psi(2S)$  branching ratio times the inclusive cross section.

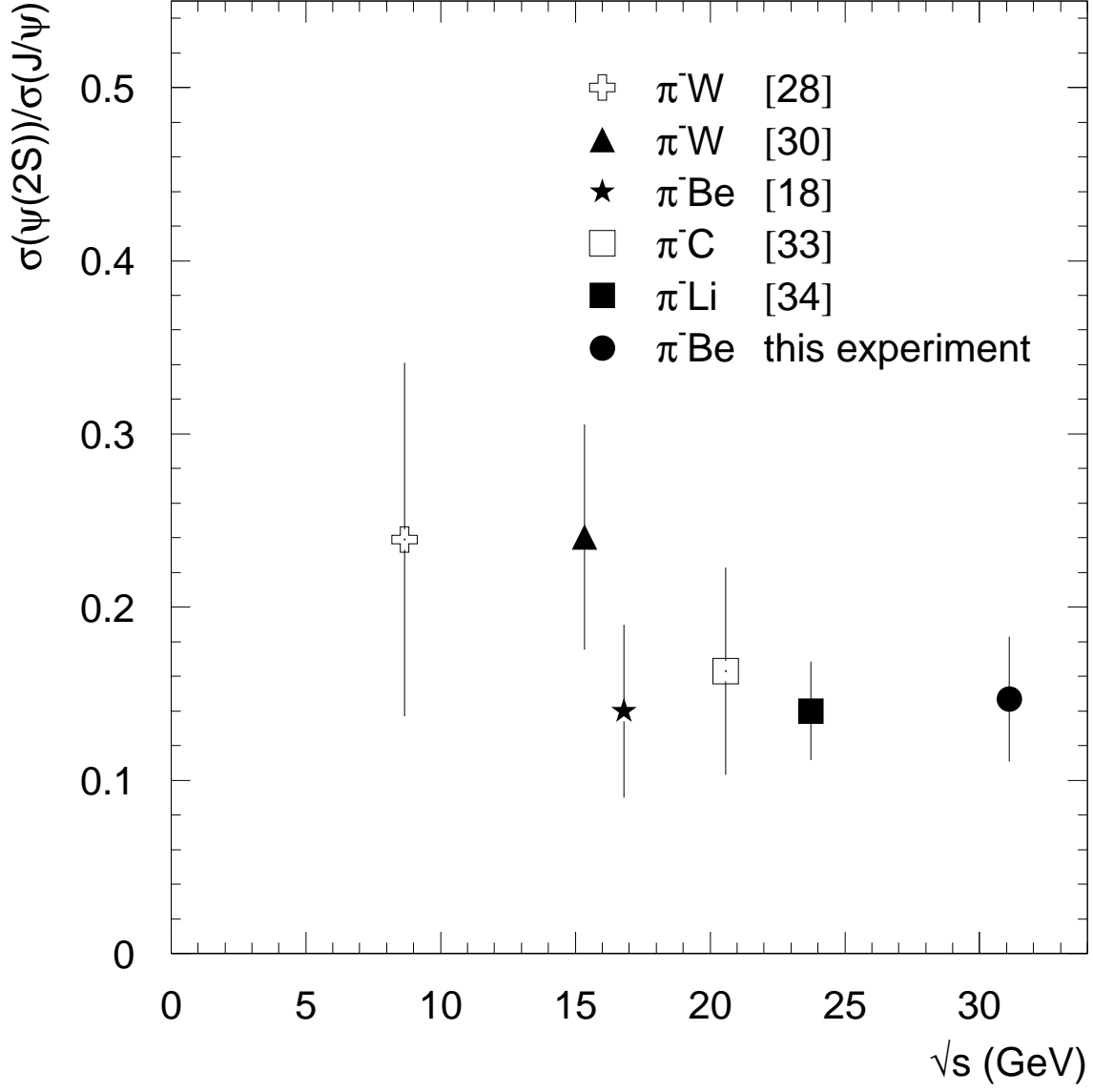


FIG. 14. Dependence of the ratio of inclusive  $\psi(2S)$  and  $J/\psi$  cross sections on  $\sqrt{s}$  for  $\pi^-$ -nucleon interactions (uncertainties are statistical and systematic added in quadrature).

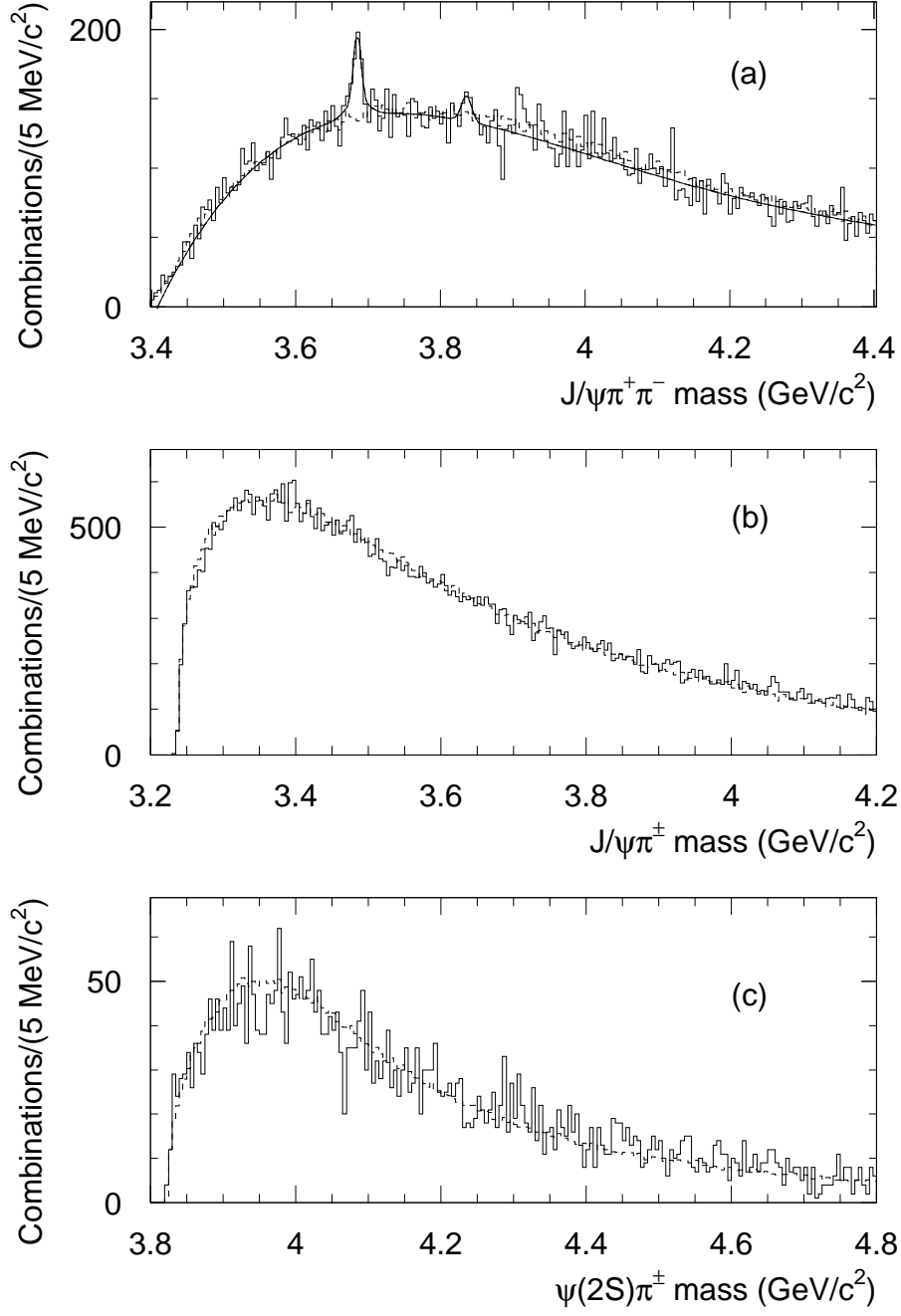


FIG. 15. The invariant mass distributions for: (a)  $J/\psi\pi^+\pi^-$ , (b)  $J/\psi\pi^\pm$ , and (c)  $\psi(2S)\pi^\pm$  combinations. The solid curve in (a) represents a fit to the candidate “hidden” charm resonance plus background as described in the text. Dashed histograms show the mass spectra obtained by combining  $J/\psi$  or  $\psi(2S)$  and pions from different events.